Whole brain resting-state EEG dynamics: A mixture of linear aperiodic and nonlinear resonant stochastic processes

Ying Wang[a], Min Li[b], Ronaldo García Reyes[a,c], Maria L. Bringas-Vega[a,c], Ludovico Minati[a,d], Pedro A. Valdes-Sosa[a,c]

[a] *The Clinical Hospital of Chengdu Brain Science Institute, MOE Key Lab for NeuroInformation, University of Electronic Science and Technology of China, No. 2006, Xiyuan Ave., West Hi-Tech Zone, Chengdu, 611731, China*

[b] *Hangzhou Dianzi University, Hangzhou, Zhejiang, China*

[c] *Cuban Neuroscience Center, Havana, Cuba*

[d] *Center for Mind/Brain Sciences (CIMeC), University of Trento, 38123 Trento, Italy*

Abstract

A longstanding debate in neuroscience asks whether macroscale brain signals can be treated as purely linear Gaussian processes, or if they harbor intrinsic nonlinear dynamics. Here we present evidence that normal resting-state EEG signals contain robust nonlinearities, which appear to be concentrated in specific oscillatory components. To investigate this, we introduce BiSpectral EEG Component Analysis (BiSCA), a novel spectral modeling framework that unifies power spectral and bispectral analysis to identify inter-frequency harmonic relationships and distinguish distinct signal components. Unlike prior spectral parameterization approaches, BiSCA is designed to explicitly test for nonlinearity. Crucially, simulations confirm its ability to separate true nonlinearity from non-Gaussianity - a common confound where linear, non-Gaussian systems can produce diffuse bicoherence that might be mistaken for nonlinear interaction. We performed a nonlinear, non-Gaussian test for two large datasets of human brain recordings (1,771 intracranial EEG channels and 960 scalp EEG recordings), and with the BiSCA model we were able to apply the tests on each identified component, revealing a clear organizational principle within these signals. We found that the brain's broadband, aperiodic background (the ξ (Xi) process) behaves predominantly as a linear, Gaussian process. In contrast, the narrowband oscillatory ρ (Rho) components - including the prominent alpha (α) rhythm and other spectral peaks - are the primary source of cortical nonlinearity, exhibiting significant quadratic coupling. In fact, over two-thirds of all EEG and iEEG channels showed significant departures from linear Gaussian behavior, challenging a frequent assumption of widespread linearity in large-scale brain signals. Notably, we observed a striking dissociation between signal power and nonlinearity. While the occipital alpha (α) rhythm dominates the EEG power spectrum, the strongest nonlinear signatures arose from the parietal mu (μ) rhythm. These

findings suggest that nonlinear resonance phenomena are pervasive in cortical signals, arising primarily from the brain's resonant neural oscillations rather than its aperiodic activity. Our work demonstrates the utility of bispectral methods for characterizing complex brain dynamics and underscores that even at the macroscale, our understanding of neural activity will remain incomplete without accounting for these intrinsic nonlinear interactions.

Highlights

BiSCA method: Introduces BiSpectral EEG Component Analysis, a new approach that combines power spectrum and bispectrum analysis to identify harmonic frequency relationships and detect nonlinear resonance in EEG data.

Linearity and Gaussianity testing: The study introduces a robust statistical framework modifying the classic Hinich test. Using median- and maximum-based statistics derived from the bicoherence's asymptotically complex Gaussian distribution, this approach directly tests each EEG component's linearity and Gaussianity, separating truly linear signals from those exhibiting higher-order nonlinear interactions.

Widespread nonlinear dynamics: Large-scale analysis of resting-state brain activity (1,771 rs-iEEG channels, 960 scalp rsEEG recordings) reveals that the majority of recordings (>2/3) exhibit significant deviations from linear Gaussian behavior, contrary to the assumption that macroscopic signals are predominantly linear.

Aperiodic vs. oscillatory processes: The broadband Xi (ξ) component of the EEG (aperiodic 1/f background) is identified as largely linear and Gaussian, whereas the rhythmic Rho (ρ) components (e.g. alpha oscillations) are the primary sources of nonlinear coupling, generating significant bicoherence and higher-order interactions.

Nonlinear resonance in brain rhythms: Evidence of quadratic nonlinearity (harmonic and intermodulation peaks in the bispectrum) is especially pronounced for specific oscillations. For example, the alpha rhythm exhibits clear harmonic coupling, and the sensorimotor mu rhythm produces the strongest nonlinear signature despite its moderate power.

Spatial and theoretical implications: There is a striking dissociation between spectral power and nonlinearity across the cortex – occipital alpha dominates power, but parietal regions (mu rhythm)

maximize nonlinearity – highlighting that strong oscillatory power does not equate to linearity. These results affirm that nonlinear interactions are an intrinsic aspect of large-scale brain activity, informing theories of brain dynamics and guiding future development of models that integrate both linear and nonlinear elements.

1. Introduction

A pivotal debate in neuroscience centers on whether mesoscale brain dynamics, as reflected in resting state EEG (rsEEG) and fMRI (rsfMRI), can be described entirely as linear, Gaussian stochastic processes. Recent studies, such as Nozari et al. (2024) and Raffaelli et al. (2024), argue that linear time series models suffice, suggesting that the intricate nonlinearities observed at the microscale - within neurons, synapses, and neural masses - are effectively "averaged out" at larger scales. This hypothesis carries profound implications: if true, it would imply that mesoscale signals lack observable nonlinear signatures, limiting our ability to infer microscale dynamics from macroscopic measurements.

Given the high temporal resolution of the scalp or intracranial resting-state EEG (rsEEG) (Figure 1a), which makes it particularly suitable for investigating dynamic neural processes, reports asserting linearity or Gaussianity are somewhat surprising since substantial evidence indicates that nonlinear dynamics are observable in rsEEG signals. Nonlinear dynamics in neural systems, as evidenced by phenomena in the frequency domain such as nonlinear resonance, cross-frequency coupling (CFC), and phase-amplitude coupling (PAC), are critical for understanding the complex oscillatory interactions observed in resting-state EEG (rsEEG) and task-related EEG signals. One of this common feature of nonlinear neural oscillations is their non-sinusoidal waveform shape, which is abundant in human electrophysiological recordings and reflects the complex biophysical dynamics of underlying neural generators (S. R. Cole & Voytek, 2017), as modeled by early neural mass models (Lopes da Silva et al., 1976; Zetterberg et al., 1978; Grimbert & Faugeras, 2006; Spiegler et al., 2010). This non-sinusoidality, often overlooked by conventional spectral analysis that assumes sinusoidal structure, carries important physiological information and can distinguish between different behavioral states resting states (Bender et al., 2025; S. R. Cole et al., 2017; S. R. Cole & Voytek, 2017; S. Cole & Voytek, 2019). The presence of these complex waveforms has significant implications, as it inevitably generates harmonic components in the frequency spectrum (Carlqvist et al., 2005; Donoghue et al., 2022; Idaji et al., 2022; Klimesch, 2012; Labecki et al., 2016, 2016; Mohsini et al., 2017; Roberts & Robinson, 2012; Schaworonkow, 2023; Van Albada & Robinson, 2013a), and this asymmetric nonlinearity or quadratic phase coupling is able

describe by bicoherence (Lopes da Silva et al., 1976; Bartz et al., 2019). Subsequent theoretical and empirical work by Nolte and colleagues demonstrated the mathematical equivalence between phase-amplitude coupling measures and bispectral analysis, providing a unified framework for understanding nonlinear resonance in neural systems (Zandvoort & Nolte, 2021). Furthermore, large-scale brain network models have shown that cross-frequency coupling emerges naturally from the nonlinear dynamics of interconnected neural populations, supporting the view that nonlinear resonance is a fundamental organizing principle of brain activity (Jirsa & Müller, 2013). Critically, if macroscopic signals were limited to low-order statistical properties (e.g., mean, variance), none of these nonlinear resonance phenomena would have been observed, and widely and successfully used techniques like Independent Component Analysis (ICA) - which relies on higher-order moments - would fail to separate signal sources.

The debate whether the EEG are linear or nonlinear can be resolved by recognizing that various neural phenomena - including phase coupling, intermodulation, and harmonic generation - can be unified under the theoretical framework of nonlinear resonance. Nonlinear resonance comprehensively explains the complex dynamics observed in neural systems, bridging the gap between microscale nonlinearities and macroscale observations.

This debate is obfuscated by ignoring a critical distinction between linearity - the functional form of a system's temporal evolution, governed by superposition - and Gaussianity - the statistical distribution of its variables. A linear system, such as an autoregressive model, can yield non-Gaussian outputs if driven by non-Gaussian inputs (e.g., skewed or heavy-tailed noise). Conversely, a nonlinear system may produce approximately Gaussian statistics when nonlinear effects are subtle or mimic the summation of many independent components, approximating a Central Limit Theorem scenario. However, strongly nonlinear systems frequently exhibit pronounced non-Gaussianity, such as multimodal or skewed distributions - especially when involving harmonic coupling or multiplicative feedback. Thus, neural dynamics can embody any combination of linearity/nonlinearity and Gaussianity/non-Gaussianity, necessitating careful separation of these concepts in EEG analysis.

It is also important to recognize that the EEG signal is a mixture of different types of processes and that Gaussianity or linearity (or their absence) may vary across these processes. Understanding the differential properties of distinct EEG components is crucial to our analysis, as it allows for a more nuanced interpretation of the underlying neural mechanisms. By dissecting the contributions of various

subprocesses - such as oscillatory rhythms, aperiodic activity, and noise - it becomes possible to identify which components adhere to linear dynamics and Gaussian statistics and which deviate due to nonlinear interactions or non-Gaussian inputs. This component-specific approach not only refines our understanding of EEG generation but also enhances the accuracy of macroscale models in capturing microscale dynamics.

One very successful strand of research for decomposing the EEG into processes is based on the EEG second-order cumulant $S(f)$ or spectrum for frequency f. This is a logical choice since, for strictly stationary processes without long-term memory (Brillinger, 2001), the distribution of optimized estimators $\hat{S}(f)$ (for example, with Multitaper) and completely characterizes linear time-invariant signals driven by noise. Figure 1b illustrates the separation of an EEG $\hat{S}(f)$ into distinct components defined by simple functional forms, each determined by only a few parameters, an approach known as **Spectral Parameter Analysis** (**SPA**) (Appendix A.2). An early example of SPA is Pascual-Marqui et al. (1987), who proposed the Xi-Alpha (ξα) model. They showed that EEG spectra have two dominant components: an aperiodic Xi (ξ) component and multiple peaks characterizing rhythmic activity (which we will call generically Rho components or ρ), the best known being the Alpha (α) component (the Peak 1 in Figure 1b). The FOOOF model is a recent example of SPA (Donoghue et al., 2020). Not only do these components have important behavioral correlates (Connor, 2022; Dragovic et al., 2022; McKeon et al., 2024), but they also ignited research into their distinctive physiological underpinning (Brake et al., 2024a; Kramer & Chu, 2024).

However, SPA, which relies on second-order moments (the power spectrum), provides a sufficient characterization only for characterizing linear Gaussian systems. For such systems, all higher-order cumulants are zero, rendering methods based on them unnecessary. Consequently, SPA is thus blind to nonlinear dynamics. For this type of activity, higher-order spectral tools, such as the bispectrum $B(f_1, f_2)$ and its normalized version, the bicoherence $b(f_1, f_2)$, between frequencies f_1 and f_2, are required to detect phenomena like harmonic generation, phase coupling, or other nonlinear interactions. Notably, this underscores that only testing the marginal Gaussianity of a signal is insufficient to detect nonlinearity since many nonlinear systems can generate marginal distributions indistinguishable from Gaussian. Analysis of nonlinear time series (multiple lags) is needed. Another fundamental problem of state-of-the-art SPA is that the harmonic relationships between second-order spectral peaks are not explicitly modeled despite their being ubiquitous in EEG recordings.

We introduce BiSCA (**BiS**pectral EEG **C**omponent **A**nalysis), a generalized model of EEG spectral components designed to detect and quantify nonlinear resonance and address the limitations of current spectral analysis models. Unlike traditional approaches focusing solely on isolated second-order spectral peaks, which is phase blind, BiSCA provides a combined model specifically designed to identify nonlinear resonance phenomena in neural signals, allows modeling harmonically related second-order peaks and their corresponding bispectral counterparts. This extension allows for a more comprehensive characterization of EEG activity. Furthermore, BiSCA parameter estimation is based on maximum likelihood, enabling direct statistical testing of linearity and Gaussianity for each component. We show these components for one case in (Figure 1 e-g). We note that the present version of the model is for a "quasi-stationary" EEG time series. A time-resolved BiSCA in the spirit of (Wilson et al., 2022a) is a straightforward work in progress. We also defer to other paper the issue of nonlinearity of brain connectivity.

In the second part of our paper, we demonstrate how the BISCA model reveals substantial nonlinearities and non-Gaussian characteristics in EEG data using 1,771 resting-state intracranial EEG (iEEG) recordings from 106 patients. In contrast to the hypothesis that such nonlinearities are averaged out in the coarser scalp recordings, we show this is not the case using 960 healthy individuals' EEG resting-state scalp (rsEEG) recordings.

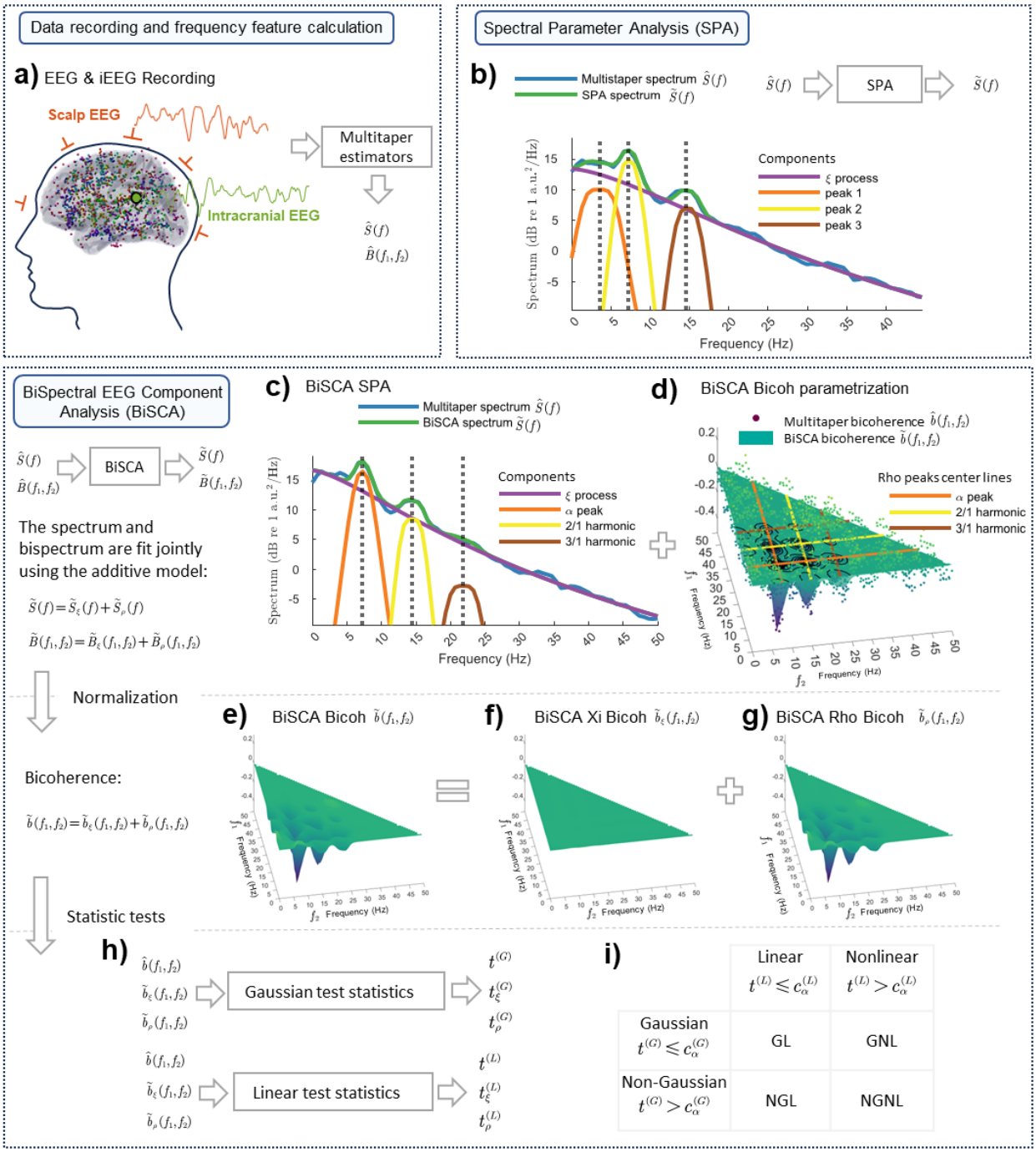

Figure 1: Uncovering rsEEG nonlinearity and non-Gaussianity with BiSCA (BiSpectral Components Analysis)*. (a) We obtain for intracranial EEG (iEEG) and resting state EEG the Multitaper Spectral and Bispectral Estimators, $\hat{S}(f)$ and $\hat{B}(f_1, f_2)$ which are data summaries. (b) SPA (Spectral Parameter Analysis) decomposes $\hat{S}(f)$ as a linear superposition of individual peaks (color-coded lines) to produce a SPA model spectrum $\tilde{S}(f)$. The BiSCA model (c)-(g) designed to parametrize nonlinear resonances through joint modeling spectrum and bispectrum($\hat{S}(f)$ $\hat{B}(f_1, f_2)$) analysis to producing BiSCA spectral and bispectral estimators $\tilde{S}(f)$ and $\tilde{B}(f_{1,2})$; (c) Spectral data $\hat{S}(f)$ and BiSCA $\tilde{S}(f)$ fits that model harmonic relationships; (d) Data of the Real part of the*

bicoherence $\hat{b}(f_1, f_2)$ and BiSCA model fits $\tilde{b}(f_1, f_2)$. Bicoherence is the normalized version of the bispectrum. Lines for the harmonics shown in (c) are superimposed on the f_1-f_2 plane are Additive decomposition of BiSCA bicoherence (e-f), with (e) total bicoherence, (f) bicoherence of Xi-component, and (g) bicoherence of Rho-component; In (h), these bicoherence used to calculate the statistic for the non-Gaussian and nonlinear test; (i) the table classifies the signal by comparing to the critical value of Gaussianity and Linearity test, a signal is classified as Gaussian if $t^{(G)} \leq c_\alpha^{(G)}$ and Linear if $t^{(L)} \leq c_\alpha^{(L)}$; otherwise, it is classified as Non-Gaussian or Nonlinear, respectively.

2. Results

2.1 Simulation of asymmetric EEG waves

The bicoherence reveals more clearly quadratic interactions between harmonics, which are of particular interest to use since they reveal the asymmetry of EEG waveforms as shown in Figure 2. Figure 2a shows an example of the standard EEG variant known as "wicket waves" (Marcuse et al., 2015), which are very asymmetrical. In this simulation a 2.5-second iEEG segment of a Wicket wave fitted by a Nonparametric Nonlinear Autoregressive (NNAR) model and pruned to define the core dynamics. With this NNAR model we can produce long-running simulations of two types. Figure 2b shows a simulation modification that symmetrizes the synthetic waveform, generated by enforcing odd symmetry ($F(-\boldsymbol{x}) = -F(\boldsymbol{x})$, details in appendix). By contrast, in Figure 2g, we show the simulation that preserves the asymmetry of the waveforms. Each type of simulation is processed to produce its limit cycle phase portrait (2c,2h), Potential landscape (2d,2i), spectrum (2e,2j), and bicoherence (2f,2k).

The geometric representations of these two simulations reveal a stark contrast. For the asymmetric system, the potential landscape (Figure *2*i), estimated from the state-space density using kernel methods, reveals a distinctly asymmetric basin of attraction. The shape of this potential well geometrically constrains the system's trajectory. Instead of a uniform, elliptical path, the trajectory is forced to follow the asymmetric contour of the potential minimum. This constrained path is the distorted, non-uniform limit cycle shown in the phase portrait (Figure *2*h), which in turn corresponds to the asymmetric "wicket" morphology of the waveform in the time domain (Figure *2*g). Conversely, for the symmetric system, the estimated potential landscape (Figure *2*d) is a symmetric, concentric well. This lack of geometric constraint allows the trajectory to trace a symmetric limit cycle (Figure *2*c), corresponding to a perfectly symmetric time-domain waveform (Figure *2*b).

These geometric differences are directly explained by the underlying spectral properties. The spectrum of the symmetric system (Figure *2*e) contains only odd-order harmonics, which results in a bicoherence of zero everywhere (Figure *2*f), reflecting the complete absence of quadratic phase coupling. By

contrast, the asymmetric wicket wave simulation shows clear even and odd harmonic peaks in its spectrum (Figure *2*j). This harmonic structure produces significant phase coupling, which appears as high-valued peaks in the bicoherence plot (Figure *2*k) at the corresponding frequency pairs.

This direct visual and quantitative contrast demonstrate that geometric asymmetry in the estimated potential landscape and limit cycle is a state-space representation of the nonlinear phase coupling quantified by the bicoherence. Such behavior is inaccessible to a linear system, which is fundamentally constrained to a symmetric, parabolic potential well, producing only perfectly elliptical trajectory and exhibiting zero bicoherence.

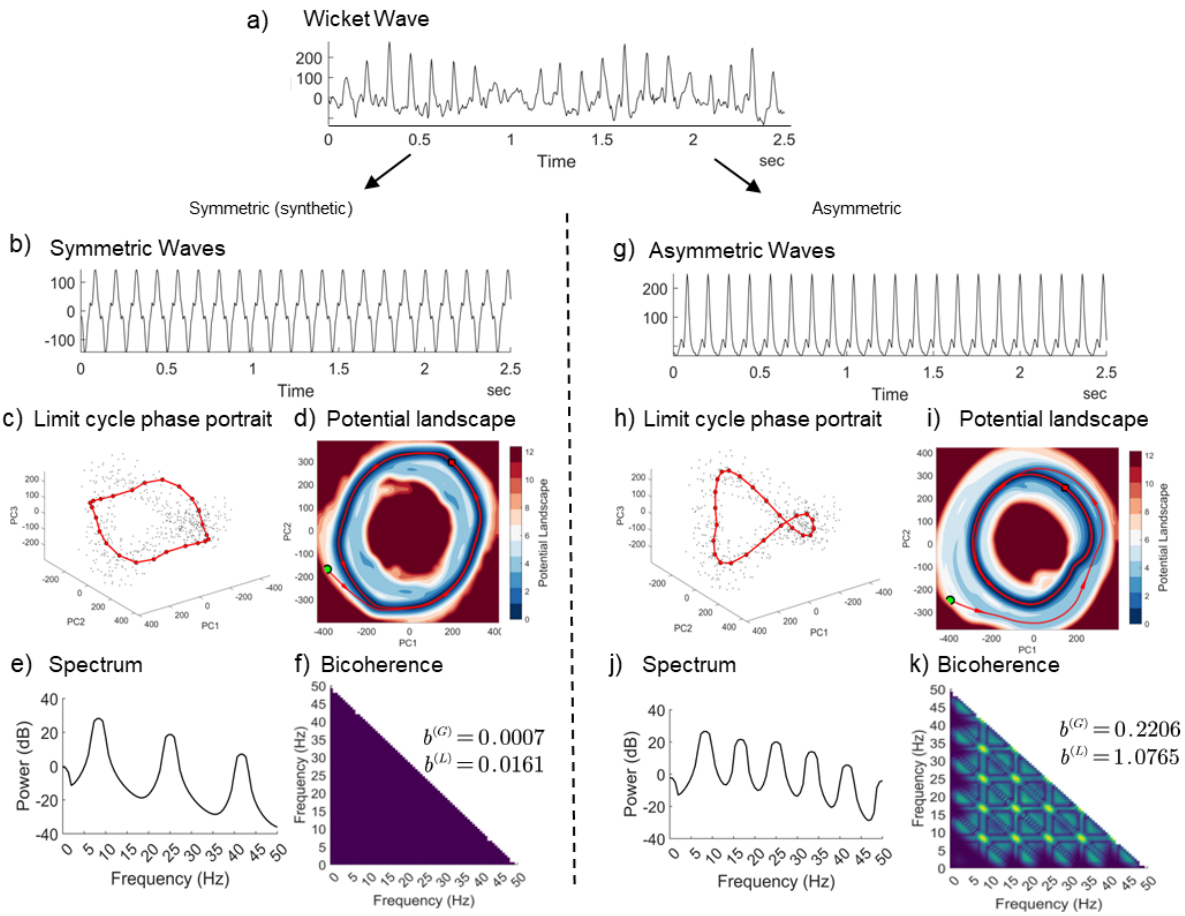

Figure 2 *Comparison of asymmetric system dynamics from iEEG data and a synthetic symmetric counterpart. The analysis begins with (a) an iEEG segment of a Wicket Spikes wave. A Nonparametric Nonlinear Autoregressive (NNAR) model is trained on this data and pruned to define the core dynamics. This model is used to simulate two cases. Left Panel (b-f): A synthetic symmetric system produces (b) a symmetric waveform, (c) a symmetric 3D limit cycle phase portrait (red line) with pruned states (used in nonparametric model, coreset, gray dots), and (d) a symmetric 2D potential landscape. The corresponding (e) spectrum contains only the fundamental frequency and its odd-order harmonics, and the (f) bicoherence is zero. Right Panel (g-k): The original asymmetric system dynamics are simulated from the model. This yields (g) an asymmetric waveform, (h) an asymmetric limit cycle, and (i) an asymmetric potential well. The (j) power spectrum contains the fundamental frequency (around 8.7 Hz) plus its*

even and odd harmonics, and the (k) bicoherence shows non-zero peaks at frequency pairs involving the fundamental and its harmonic components.

2.2 Nonlinear and non-Gaussian cortical dynamics in EEG/iEEG revealed by Bicoherence.

We assessed linearity and Gaussianity for the quasi-stationary EEG and iEEG data using the modified Hinich test (Hinich, 1982) based on the Multitaper Bicoherence $\hat{b}(f_1, f_2)$, with a threshold adjusted using the Benjamini-Hochberg FDR procedure (q=0.001). The results of these tests are presented in Table 1, classified as depicted in Figure 1i. Note that our reference to linearity or Gaussianity indicates the rejection of the null hypothesis in the corresponding tests. Despite the conservative value for q, only 14.7% of the EEG and 25.7% of the iEEG recordings tested linear and Gaussian. It is noteworthy that 81.6% of EEGs and 67.9% of iEEG recordings were either nonlinear or non-Gaussian. Very few recordings tested as linear and non-Gaussian: 3.6% for EEG and 6.4% for iEEG, respectively. The proportions of Gaussianity and non-Gaussianity for nonlinear recordings were approximately the same for both EEG and iEEG. A detailed breakdown of the test statistics from different perspectives is provided in Figure 2.

Table 1 Percentages of EEG and iEEG recordings that are Linear, Nonlinear, Gaussian or non-Gaussian

	EEG			**iEEG**		
	Linear	Nonlinear	Total	Linear	Nonlinear	Total
Gaussian	14.7	39.3	54	25.7	17.1	42.7
Non-Gaussian	3.6	42.3	46	6.4	50.9	57.3
Total	18.4	81.6	100	32.1	67.9	100

Topographic maps (Figure 3a and 3c) illustrate the interpolated proportion of different test results across electrodes, highlighting distinct topographic distributions. For EEG test results (Figure 3a), linearity (Gaussian or not) is classified most frequently at central electrodes. In contrast, iEEG shows that Gaussianity and linearity are predominant in the frontal region, while non-Gaussianity and linearity are frequent in the occipital area but less so in the right frontal area (Figure 3c). Though Gaussianity and nonlinearity both EEG expresses highly in the frontal areas, it seems absent in the iEEG. EEG recordings reveals an anterior-to-posterior increase, peaking at occipital electrodes. In contrast, iEEG is mainly central, with asymmetric distribution in the occipital lobes, predominantly on the right.

An alternative perspective is offered by plotting the proportion of test result types over the triangular bifrequency domain (f_1, f_2) and $f_1 + f_2 \leqslant 50\,\mathrm{hz}$ (corresponding to the bicoherence principal domain,

here after bifrequency panel) (Figure 3b,3d). Note that here, though we deal with statistics for each (f_1, f_2) pair, the threshold for deciding tests is the global one for the whole triangular plane, corrected for FDR. Also, by construction, the Gaussianity threshold $c_\alpha^{(G)}$ and the linearity threshold $c_\alpha^{(L)}$ are related as $c_\alpha^{(L)} > c_\alpha^{(G)}$, for individual tests, resulting in a zero proportion of nonlinear but Gaussian results (lower left of Figures 2 b and d). A diagonal ridge of Non-Gaussian Linear test results suggests time domain asymmetries of waveforms for all frequencies. Note, however, the off-diagonal bands of interference coupling for the Alpha frequency harmonics suggest frequency doubling and intermodulation effects. Note the localized bicoherence peak at (10 Hz, 10 Hz) associated with Nonlinearity and Non-Gaussianity. This result indicates evidence of intra-band nonlinear coupling in the alpha rhythm. The iEEG (Figure 3d) shows test proportion on the frequency triangle like those in Figure 3b for the EEG. However, the distribution of the iEEG test proportions seems more smeared on the frequency triangle when compared to scalp EEG data.

It is instructive to view the topographies of the peak frequencies at which the spectrum is maximum, $f_{S_{\max}} = \underset{f}{\operatorname{argmax}}\,(S(f))$, and the frequency at which the bicoherence is maximal, determined using the maximum of the main diagonal bicoherence $f_{b_{\max}} = \underset{f'}{\operatorname{argmax}}\,(b(f', f'))$, indicates that where the frequency-doubling occurs. The latter is restricted to the bispectral values on the main diagonal of the principal domain. The occipital and parietal areas are in the alpha band, while the frontal region slows down to the theta band. The peak frequency of the bicoherence is higher than the peaks found by the spectrum.

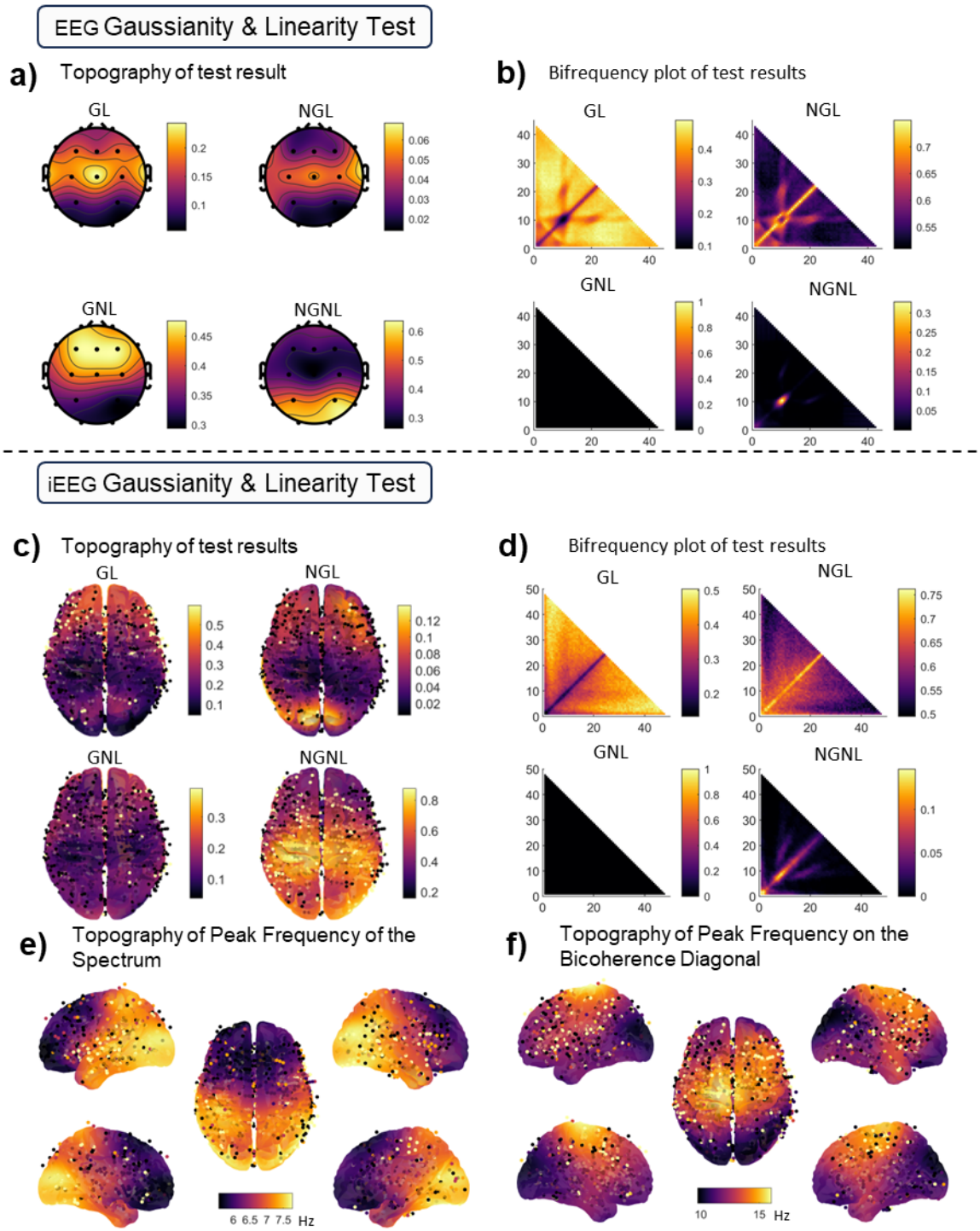

Figure 3. ***This figure presents the results of Gaussianity and linearity tests applied to iEEG and scalp EEG recordings.*** *(a) The topography map of the proportion of test classes of EEG data; (b) the proportion of test class of EEG along the bifrequency panel; (c) the surface plot interpolated by the statistical test result (0: accept, 1: reject) of iEEG channels; (f) the proportion of test class of iEEG along the bifrequency panel; (c-d) the spatial distribution of the frequency for the maximum spectrum peak and bicoherence peak after removing the Xi trend.*

2.3 Nonlinear resonances manifest in Rho peaks, while the Xi process remains linear and Gaussian

Besides identifying the non-Gaussianity and nonlinearity of the complete signal, we apply the statistical test to each component separated by the BiSCA model. From now on we report only the analysis of iEEG data since it is important to study issues in the absence of large volume conduction effects.

Figure 4a shows the distribution of the Gaussianity test $b^{(G)}$ statistics for each component relative to the significance threshold. The $b^{(G)}$ of the full signal is located around the threshold, while the statistics for the aperiodic Xi process $b_{\xi}^{(G)}$ and periodic Rho processes $b_{\alpha}^{(G)}$ are much lower than the threshold, indicating less evidence of non-Gaussianity than in the composite signal. The right subplot (Figure 3b) shows the bicoherence statistic $b^{(L)}$ for nonlinearity. The $b^{(L)}$ of full signal and the $b_{\alpha}^{(L)}$ of Rho processes are much higher than the threshold, indicating significant nonlinearity. In contrast, the statistic $b_{\xi}^{(L)}$ for the Xi process rarely exceed the threshold, suggesting it behaves linearly.

An interesting question is how much tests for Linearity and Gaussianity of the whole signal are influenced by those of each spectral component. The scatterplots of the tests for both linearity and Gaussianity between the full signal and its components shed light on this issue. A clear relation exists between the two types of tests for the full signal and the Rho processes (Figure 4e). This is not the case for the Xi process (Figure 4f). Therefore, the primary factors contributing to the rejection of Gaussianity and linearity in the iEEG appear to be nonlinear resonances related to the Rho processes.

Another crucial aspect of each Spectral component is the spatial distribution of their statistical features across the brain as shown in Figure 4g-4l. The energy (sum of the power spectrum over all frequencies) of the aperiodical Xi process is broadly distributed, with notable concentrations in the occipital lobe, temporal lobe, and left parietal lobe (Figure 4g). The energy of the periodical Rho processes shows a more focal distribution, with high energy localized explicitly in the occipital lobe, corresponding to the Alpha rhythm, and an anterior-to-posterior decrease toward the prefrontal cortex with some energy in the parietal lobes corresponding to the Mu rhythm (Figure 4h). These energies have been harmonized to account for differences in EEG amplifiers and site conditions with the Incomplete Observed Linear Mixture Model (IOLMM) model (Wang et al., 2024).

Overall, the Gaussianity statistics are relatively low across space for both processes. Non-Gaussianity tests for the Xi process are higher in the frontal region, while the Rho processes have a higher value in

the occipital and parietal regions. When observing the maps for the nonlinearity statistic the two processes have distinct spatial distributions. The Xi process barely is considered nonlinear across the entire brain (Figure 4k). Conversely, the Rho processes shows notable nonlinearity in regions that also exhibit high energy, particularly in the parietal lobes (Figure 4l), and to a lesser degree in the occipital areas.

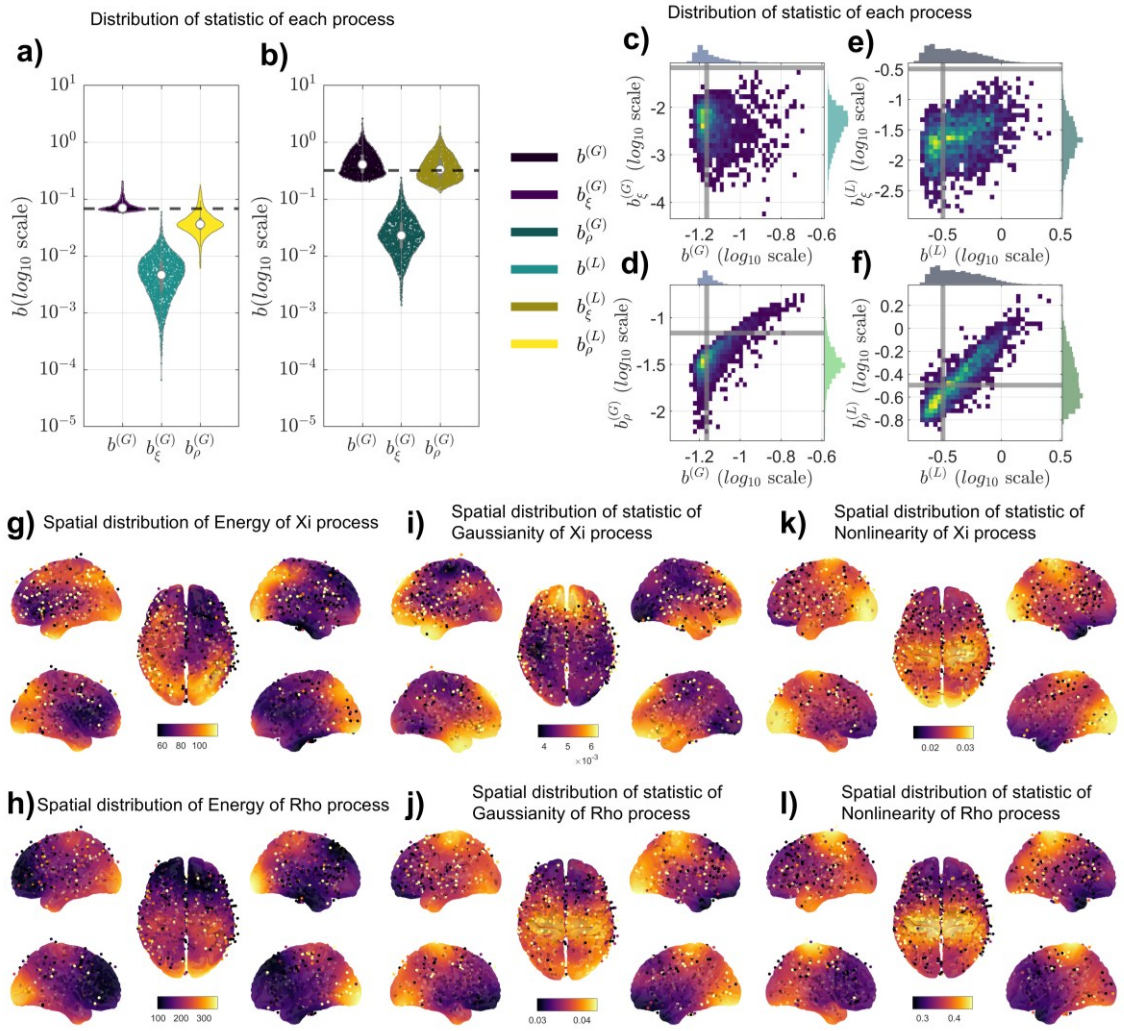

Figure 4: ***Statistical features of iEEG signals decomposed into Xi trends and periodical Rho components.*** *(a-b) Violin plots showing the distribution of the (a) Gaussianity statistic $b^{(G)}$ and (b) nonlinearity (bicoherence) statistic $b^{(L)}$ for the full signal, the aperiodical Xi process (ξ), and the periodical Rho processes (ρ). The dashed line indicates the threshold for statistical significance. (c-f) Scatter plots showing the relationship between the full signal and its components. Plots (c-d) show the correlation between the Gaussianity statistics of the full signal and the (c) Rho processes and the (d) Xi process. Plots (e-f) show the correlation between the linearity statistic of the full signal and the (e) Rho processes and the (f) Xi process. (g-l) Topographical maps of the brain showing the spatial distribution of key statistics for the aperiodical Xi and Rho processes. (g-h) Spatial distribution of energy. (i-j) Spatial distribution of the Gaussianity statistic $b^{(G)}$. (k-l) Spatial distribution of the nonlinearity statistic $b^{(L)}$. Red indicates higher values, while blue indicates lower values.*

3. Discussion

By analyzing a datasets of 1,771 intracranial EEG (iEEG) and 960 subjects of scalp EEG reveal that only a small minority of recordings can be described as both linear and Gaussian. Over 81% of scalp EEG and 67% of intracranial EEG recordings deviate from this ideal, exhibiting significant nonlinearity and/or non-Gaussianity. This directly challenges the notion that mesoscale brain dynamics are predominantly linear and Gaussian(Nozari et al., 2024; Raffaelli et al., 2024). By decomposing the iEEG signals with BiSCA, we found a clear separation between the aperiodic background activity and rhythmic oscillatory components. The broadband Xi process (aperiodic 1/f component) behaves largely as a linear, Gaussian process, whereas the narrowband Rho components (oscillatory peaks, e.g. the alpha rhythm and Mu rhythm) are the primary sources of nonlinearity in the EEG. In other words, the resonant oscillations in the brain carry nearly all of the detected quadratic nonlinear interactions (as evidenced by significant bicoherence), while the aperiodic component shows minimal nonlinear coupling. While previous SPA methods have successfully characterized the power-spectral features of these components, they are blind to phase relationships and therefore cannot assess their nonlinearity.

We observed clear signs of nonlinear resonance phenomena in the data. In the bifrequency domain analysis of the bicoherence, rhythmic peaks (especially the 10 Hz alpha rhythm) exhibited harmonic coupling – for example, frequency-doubling and intermodulation effects were visible as diagonal and off-diagonal bicoherence. These results confirm that well-known cross-frequency coupling phenomena (e.g. harmonics of alpha) are present even in resting-state activity and are quantitatively detectable with our approach. With our BiSCA model we can parameterize the coupling strength between oscillatory peaks.

3.1 Linear vs. Nonlinear Modeling Debate

Our findings directly inform the ongoing debate about whether large-scale brain signals can be treated as purely linear. Recent studies argued that macroscopic resting-state dynamics are adequately captured by linear models, suggesting that microscopic nonlinearities are “averaged out” at the EEG/fMRI level. In contrast, our results prove that nonlinear dynamics are present and measurable at the macroscale. Most EEG channels showed higher-order statistical structure (non-zero bicoherence), implying that nonlinear interactions among neural population oscillations survive spatial and temporal averaging. The presence of quadratic nonlinearities in EEG supports the view that macroscopic signals reflect microscale nonlinear mechanisms. We have shown that the percentage of scalp EEG channels

344 showing significant nonlinearity is not lower than that observed in iEEG recordings. This observation can
345 be explained by volume conduction. While a nonlinear source like the Mu rhythm originates from a
346 localized cortical area (e.g., the sensorimotor cortex), its electrical signature is not confined to the
347 overlying scalp electrodes. Instead, our finding that a greater percentage of scalp EEG channels
348 appeared nonlinear than iEEG channels suggests that rather than decreasing nonlinearity as might be
349 expected (Donoghue et al., 2022; Schaworonkow & Nikulin, 2019, 2022), volume conduction primarily
350 smears this activity across the scalp, causing the nonlinear features to be detected in a wide array of
351 channels. Prior work (Lopes da Silva et al., 1976; Zetterberg et al., 1978; Grimbert & Faugeras, 2006;
352 Spiegler et al., 2010; S. R. Cole et al., 2017; S. R. Cole & Voytek, 2017; S. Cole & Voytek, 2019;
353 Bender et al., 2025) showed that nonlinear phenomena like cross-frequency coupling and harmonic
354 generation can occur in neural mass models and actual EEG/LFP recordings. Our empirical evidence
355 builds on this, suggesting that large-scale measures retain higher-order structure reflecting nonlinear
356 resonance in neural circuits. This finding suggests a re-examination of macroscale neural modeling: to
357 capture brain dynamics fully, it may be necessary to incorporate nonlinear terms. The debate should
358 thus move beyond the binary question of "linear vs. nonlinear models" and consider how specific
359 nonlinear features (like those we observed in Rho oscillations) can be integrated into interpretable
360 models of brain activity. It would therefore be premature to assert the superiority of linear models
361 (Nozari et al., 2024) without optimally tuning and evaluating nonlinear models on an equal footing.

362 **3.2 Interpretation of Oscillatory vs. Aperiodic Components**

363 The biophysical separation (Pascual-Marqui et al., 2022) of components in BiSCA follows the assumption
364 that two processes are additive and independent, they come from different layers of the cortex (Silva et
365 al., 1991; Van Kerkoerle et al., 2014; Mendoza-Halliday et al., 2024; Brake et al., 2024b; Bloniasz et al.,
366 2024), represent different network activity. A recent study provides further neurophysiological evidence
367 for biophysical separation further, which demonstrated with biophysical modeling and experimental
368 evidence that Xi process is a genuine signal generated by arrhythmic network activity, rather than
369 merely an artifact of overlaid brain rhythms (Brake et al., 2024a).

370 The analytical separation of components in BiSCA is theoretically grounded in two principles. First, for
371 statistically independent processes, the cumulant spectrum (including the bispectrum) is additive
372 (Brillinger, 2001). Second, and more broadly, even for single nonlinear systems described by Volterra
373 functional series (Marzocca et al., 2008; Nichols et al., 2009), the bispectrum can be expressed as a sum

of additive frequency components. Each component is analytically defined by the system's linear and quadratic transfer functions, allowing for the formal description and identification of nonlinear interactions.

Linear Aperiodic Process (Xi): A central finding of our study is that the aperiodic (Xi, ξ) component of the EEG signal - which is widely considered to exhibit a 1/f-like power law - is predominantly linear. At first glance, this observation may appear to challenge established theories where 1/f spectra can arise from nonlinear dynamics such as self-organized criticality. However, our conclusion is not a universal claim about the origin of all 1/f processes, but rather a specific, data-driven insight into large-scale neural dynamics. The Xi component, corresponding to the continuous 1/f-like background, showed negligible bicoherence and near-Gaussian amplitude statistics across the cortex. This suggests that the aperiodic background can be modeled as a superposition of many independent or weakly interacting sources (consistent with a linear Gaussian process). In practical terms, the 1/f component likely reflects aggregate synaptic and neuronal activity that, when summed over large populations, obeys the Central Limit effect and lacks strong phase coupling. Our results empirically validate the common assumption that this broadband “noise floor” of the EEG is relatively featureless and additive – an important baseline when isolating oscillatory dynamics.

Our BiSCA framework reveals that the macroscopic EEG signal is a composite of distinct processes. This means the brain's nonlinearity is not absent; it is instead compartmentalized within the resonant (Rho) oscillations. The linearity of the Xi component can thus be understood as an emergent property, likely arising from the superposition of numerous weakly correlated neural sources where nonlinearities are averaged out at the macroscopic scale. This empirical finding is strongly corroborated by recent theoretical models. For instance, Kramer & Chu, (2024) demonstrated that a general, noise-driven dynamical system, when linearized around a stable equilibrium, naturally generates spectra with 1/f-like characteristics. This mechanism is conceptually identical to a basic linear filter in control theory, whose characteristic Bode plot slopes produce such power-law spectra, offering a parsimonious explanation. It provides a compelling theoretical foundation for why a macroscopically linear stochastic process can produce the observed aperiodic background without invoking complex nonlinear mechanisms. It is also crucial to consider the specificity of our methodology; the bicoherence is a powerful tool for detecting quadratic nonlinearity, and our results show a definitive lack of such second-order interactions in the Xi component. While we cannot formally exclude other, more complex forms of nonlinearity, our work robustly refines the debate on neural linearity. In summary, within resting-state EEG, the aperiodic

background behaves as a linear stochastic process, while significant, measurable nonlinearity is robustly confined to the oscillatory Rho components.

Nonlinear Oscillatory Components (Rho): In stark contrast, the Rho components (distinct spectral peaks corresponding to oscillatory neural generators) displayed robust nonlinear signatures. For the alpha rhythm (around 10 Hz) and other peaks, we found significant bicoherence indicating phase-locked interactions, such as harmonics (e.g. 20 Hz, 30 Hz components related to alpha) and possible subharmonics or cross-frequency coupling with other bands. The fact that the full EEG signal's nonlinearity closely tracked that of the Rho component (and not Xi) implies that oscillatory networks are the loci of nonlinear dynamics. Mechanistically, this may reflect the intrinsic properties of neural nonlinear resonances: oscillatory circuits (e.g., thalamocortical loops for alpha, sensorimotor cortex for mu) can engage in feedback and coupling that produce distortions of the sine-wave, whereas broadband activity lacks such structure.

Dissociation Between Power and Nonlinearity: An intriguing observation is the mismatch between where the strongest oscillations occur and where the strongest nonlinear effects are generated. Specifically, while the occipital alpha (α) rhythm is by far the dominant peak in the power spectrum (particularly in eyes-closed resting EEG), it was the parietal mu (μ) rhythm (an 10 Hz sensorimotor oscillation) that showed the highest bicoherence values. This spatial dissociation suggests that a large amplitude does not necessarily equate to high nonlinearity. Alpha oscillations in the visual cortex, though powerful, may behave in a relatively sinusoidal (near-linear) manner, possibly due to highly regular pacemaker dynamics. In contrast, mu rhythms – often weaker in power – exhibited disproportionately strong nonlinear interactions, perhaps indicating more complex waveform shapes or coupling with other frequencies (e.g., harmonics or sensorimotor beta rhythms). This observation is consistent with Frauscher et al., (2018), who reported that there is power peaks coexist in Alpha and Beta band in the parietal lobe, while only peaks in Alpha band appear in the occipital lobe. Our bicoherence analysis, however, advances these findings by pinpointing more specific, functionally distinct sources of nonlinearity. This dissociation between the spatial patterns of power and bicoherence is corroborated by similar EEG source-reconstruction study (Shahbazi Avarvand et al., 2018).This finding underscores that different neural generators have different dynamical regimes: some operate mostly linearly (despite high power), while others inject significant nonlinear distortion into the EEG. Recognizing this can help target specific brain networks when investigating nonlinear connectivity or when developing biomarkers based on signal complexity.

3.3 Methodological advantages

Advantages of BiSCA: Methodologically, our introduction of BiSCA (BiSpectral EEG Component Analysis) provides a framework to explicitly capture these observations. Traditional spectral parameterization approaches (SPA, e.g. FOOOF) fit EEG power spectra with parametric curves but assume linearity/Gaussianity, leaving any nonlinear structure unmodeled. BiSCA addresses this by jointly modeling the power spectrum (second-order structure) and the bispectrum (third-order structure), thereby detecting inter-frequency phase coupling and harmonic relationships that SPA would miss. A key strength of BiSCA is its use of maximum-likelihood estimation for component parameters, which enables formal statistical testing of each component's linearity and Gaussianity. This allowed us to rigorously quantify how much each component deviates from linear Gaussian assumptions, rather than relying on qualitative measures of waveform shape. We believe this approach can be broadly useful in EEG analysis, offering a more comprehensive characterization of neural signals by incorporating higher-order statistics.

Simulation Validation: In developing BiSCA, we verified on simulated data that the method can disentangle nonlinearity from non-Gaussianity. For example, a linear but heavy-tailed (non-Gaussian) signal produces a diffuse, low-amplitude bicoherence pattern, whereas a nonlinear but Gaussian (in distribution) oscillator yields sharp, localized bicoherence peaks. These simulations give confidence that our empirical findings truly indicate nonlinear coupling and are not false positives due to mere non-Gaussian noise. They also demonstrate BiSCA's specificity: it responds to genuine phase-locking between frequencies rather than incidental amplitude distribution quirks.

3.4 Methodological Limitation

Spatial Sampling and Data Considerations: Scalp EEG dataset used here includes 960 individuals recoding, come from multinational normal subjects and iEEG sample encompassed 1,771 channels across 106 patients, it is important to consider the nature of these data. The iEEG recordings come from postoperative epilepsy patients, which might have influenced the prevalence or distribution of nonlinear dynamics (e.g., due to cortical irritability or medication effects). However, we observed broadly consistent patterns between iEEG and healthy EEG, in additional, the these patterns also consistence with (Shahbazi Avarvand et al., 2018), suggesting our conclusions are not driven by pathological activity. Another consideration is the volume conduction and reference mixing in scalp EEG, which can smear true source interactions. We mitigated this by focusing many analyses on iEEG (where signals are more

focal) and by using a conservative statistical threshold (FDR q=0.001). Still, some spurious coupling in scalp recordings cannot be entirely ruled out. Future work might apply source separation or source localization before BiSCA to confirm that the identified nonlinear interactions correspond to true neurophysiological coupling rather than mixing artifacts.

We note that not all brain signals showed nonlinear features – a nontrivial minority (around 18% of EEG channels and 25%) appeared consistent with linear Gaussian dynamics. These could represent true lack of nonlinear interactions in some regions or simply reflect lower signal-to-noise ratio or insufficient data length to detect subtle effects. Caution is warranted in interpreting “absence of evidence” as evidence of absence for nonlinearity. Additionally, the statistical tests we used (modified Hinich test on bicoherence) have assumptions and might miss certain forms of nonlinearity; alternative tests or complementary measures (like phase-amplitude coupling metrics) could be applied to strengthen the evidence.

Determining the Source of Non-Gaussianity of a nonlinear system is a challenge: A methodological challenge lies in attributing the source of non-Gaussianity. This paper tries to separate the non-Gaussianity from the input and the system. The system's inherent nonlinearity and non-Gaussian innovations (e.g., stochastic inputs or noise) can contribute to deviations from Gaussianity. Nonlinear transformations of Gaussian inputs can produce non-Gaussian outputs, while non-Gaussian innovations, such as heavy-tailed or skewed noise distributions, further complicate the system's statistical properties. On the other hand, non-Gaussian innovation introduces an asymmetric distortion to the phase portrait, as seen in linear systems where deviations manifest uniformly due to the absence of state-dependent damping or recovery forces. However, in nonlinear systems, the heterogeneity of the energy landscape imposes a state-dependent constraint on these deviations. For instance, regions of strong recovery strength (e.g., steep potential wells) suppress asymmetric noise-induced perturbations more effectively than states in flatter landscape regions. This leads to a non-uniform distortion that linear assumptions cannot capture. Consequently, the diffuse background bicoherence shows reduced magnitudes in nonlinear systems Figure A 2 compared to linear counterparts, where deviations are constant across frequencies. The nonlinear case's lower bicoherence reflects the system's capacity to "filter" non-Gaussian perturbations in a state-specific manner, contrasting with the homogeneous propagation of asymmetry in linear frameworks. This distinction underscores the importance of modeling both noise non-Gaussianity and system nonlinearity when interpreting higher-order spectral features.

3.5 Implications

Nonlinear Resonance as an Organizing Principle: Our results strongly support the concept that nonlinear resonance is a fundamental organizing principle of brain activity, even at the macroscale. We empirically show that each prominent rhythm can drive nonlinear interactions (both within its own frequency band and possibly with harmonically related frequencies). This aligns with decades of theoretical work suggesting that brain oscillations do not operate in isolation but interact through nonlinear mechanisms. By explicitly linking the spectral "peaks" to bispectral evidence of coupling, we provide a more concrete basis for this principle. Going forward, this framework might help interpret phenomena like EEG cross-frequency coupling, nested oscillations (e.g. phase–amplitude coupling), and event-related harmonic responses within a unified resonance-based theory. It also suggests that modulatory relationships (such as those exploited in techniques like ICA or nonlinear signal decomposition) are inherent to brain signals and can be systematically characterized rather than treated as noise or anomalies.

Refining Macroscale Models: In practical terms, our findings encourage the development of new macroscale brain models that incorporate nonlinearity in a controlled way (Pfanzagl, 1969; Rice, 1979; Leonenko et al., 1998; Anh et al., 2004, 2007a, 2007b; Sakhno, 2014, 2020). Rather than assuming the brain is either fully linear or arbitrarily nonlinear, models might treat the aperiodic background as an additive Gaussian noise process (as linear models do) while including nonlinear coupling for the oscillatory subsystems. This hybrid perspective – essentially what our data-driven BiSCA components represent – could improve how we simulate or predict EEG dynamics. For example, large-scale neural mass or neural field models might include nonlinear feedback only in certain frequency-generating circuits (like alpha or mu generators), which could reproduce the selective nonlinearity we observed. Our work provides empirical targets for such models (e.g., the degree of bicoherence at alpha or the spatial pattern of nonlinearity) that future simulations should aim to match.

Multivariate parametric modeling to reveal the higher-order interactions: Since the brain is a coupled distributed system, as discussed by Takens' embedding theory (Takens, 1985; Stark et al., 1997), single channel observations may reconstruct the dynamic property of the whole neural system, finding from univariate analysis like this paper can provides an effective starting point for characterizing the overall state of the neural system. Nevertheless, to be more accurate, the parameterization of spectrum and bispectrum still need to be extended to multivariate to mine the cross-frequency coupling between

regions, as the previous studies on coherency (Valdés et al., 1992) and asymmetric cross-bicoherence Jirsa & Müller (2013) and source reconstruction of cross-bicoherence (Shahbazi Avarvand et al., 2018), which will help to study .the nonlinear interaction between the regions in the future. This raises a critical consideration for future connectivity analyses, as a linear systems perspective would necessitate removing harmonic effects (Idaji et al., 2022; Schaworonkow, 2023), whereas our findings suggest connectivity may be better assessed with nonlinear state-space models that treat such coupling as a feature.

Extend the BiSCA to nonstationary EEG/iEEG: This paper analyzes the system's quadratic nonlinearity (bispectrum/bicoherence) from the stationary perspective. Other nonlinear properties include multistability from a series of works in the time domain (Freyer et al., 2009, 2011, 2012) of the EEG data, which show that a linear system with a single global attractor is an insufficient model. The bicoherence approach provides a complementary perspective. As an effective tool for analysis within local, quasi-stationary windows, it can specifically identify and isolate stationary quadratic interactions that may persist across transitions between attractor states (Wang et al., 2025). This duality between stationary and dynamic perspectives underscores the complex nature of neural signals, which simultaneously exhibit both stable nonlinear features and transient dynamical shifts.

Trispectrum and higher-order nonlinearity: We limited our analysis to quasi-stationary, resting-state epochs, treating each channel's activity as statistically stationary over the recording. This was necessary for computing stable spectra and bispectra, but it leaves open the question of nonstationary or context-dependent nonlinear dynamics. Brain states vary over time; it is plausible that nonlinear coupling strengths also wax and wane (for instance, during different cognitive states or sleep stages). A time-resolved extension of BiSCA is in progress, which will allow us to track how Xi and Rho components' properties evolve moment-to-moment. Additionally, our focus on quadratic nonlinearity (third-order interactions) means we might miss higher-order effects. If there are subtle nonlinear interactions not captured by phase coupling of pairs of frequencies (for example, triple products or more complex waveform distortions), these would not be detected by bicoherence. However, many known EEG nonlinear phenomena (harmonics, cross-frequency coupling, asymmetries in waveform shape) do manifest at the third order, so bicoherence is a logical starting point. In the future, expanding to higher-order spectral analysis (e.g. Trispectrum) could reveal even richer nonlinear dynamics, though at the cost of greater data requirements and complexity.

4. Conclusion

This study provides extensive empirical evidence that nonlinearity, specifically arising from rhythmic brain oscillations, are present in macroscale neural dynamics. Large-scale brain signals cannot be adequately characterized by purely linear Gaussian models. Intrinsic nonlinear resonances linked to specific brain rhythms, like Alpha and Mu oscillations, are prominent in cortical activity.

Our BiSCA framework, introduced here, allows systematic differentiation between linear, Gaussian background processes and nonlinear resonant components.

Moving forward, fully acknowledging these nonlinearities in EEG dynamics have the potential of enhancing our understanding of brain function, informing clinical EEG applications, and encouraging the integration of more realistic dynamics into large-scale neural models. By building upon these findings, future work may offer deeper insights into the relationships between microscale nonlinear neuronal phenomena and their observable macroscale counterparts, contributing incrementally yet meaningfully to the broader field of neuroscience.

5. Materials and Methods

5.1 Materials

We used the resting EEG dataset from 960 healthy participants from the globally diverse HarMNqEEG dataset (Li et al., 2022). Participants were selected from normative or control groups, excluding those with neurological/psychiatric conditions. EEG recordings consisted of eyes-closed resting-state data. For all subjects, 18 channels were included (excluding Pz) from the 10-20 system after average referencing. Samples recorded for less than 1 minute, such as the Medicid-4-Cuba-2003, were excluded. Preprocessing involved converting signals to an average reference, segmenting data into 2.56s epochs (0.39 Hz resolution), and overlapping segments to have 157 segments per subject to maintain consistency with the iEEG data. We retained segments only if artifact-free, with no interictal discharges or slow-wave anomalies.

For Resting-state Intracranial EEG (iEEG), we used the dataset of eyes-closed resting-state wakefulness recordings, sEEG/ECoG recordings from the Montreal Neurological Institute iEEG atlas (Frauscher et al., 2018). These iEEGs were recorded from 106 patients with refractory focal epilepsy (1,772 electrodes), ensuring that tracings retained were from non-lesional, non-seizure onset zones, free of interictal

discharges, slow-wave anomalies, or post-seizure/stimulation effects. Preprocessing involved bandpass filtering (0.5–80 Hz), down-sampling to 200 Hz, and removing zero values. The study focused on 60-second eyes, in order to be consistent with the EEG data set.

5.2 Method

5.2.1 Multitaper Estimator for the Spectrum

Each segment of the signal was subjected to a Discrete Fourier transform $X(f) = \frac{1}{N_t}\sum_{n=0}^{N_t-1} x[n]e^{-j2\pi fn}$, where N_t is number of time points for each epoch. To balance the frequency resolution and computational resources, in our study, the window size was 300 time points (1.5 seconds) segments. To estimate the power spectrum, $S(f) = \mathrm{E}[X(f)X^*(f)]$ we used overlapped segments by 75% and also applied the Multitaper method, which creates windowed versions of the original time signal $x_k(n) = x(n)v_k(n)$ (Thomson, 1982; He & Thomson, 2010) in order to reduce frequency leakage bias and increase the consistency of the spectral estimate, k is the index of taper. For this purpose, we used the Sine tapers v_k (Riedel & Sidorenko, 1995) to diminish amplitude bias further. The resulting estimation procedure is then:

$$X_{k,e}(f) = \frac{1}{N_t}\sum_{n=0}^{N_t-1} x_{k,e}(n)e^{-j2\pi fn} \tag{1}$$

$$\hat{S}_k(f) = X_{k,e}(f)X^*_{k,e}(f) \tag{2}$$

$$\hat{S}(f) = \frac{1}{U_2}\sum_{k=0}^{K-1} \hat{S}_k(f) \tag{3}$$

where $U_2 = K/N_t$. In this paper, we use $NW = 1.5$, i.e. $K = 2NW - 1 = 4$ for the recordings. NW This critical parameter controls the estimator's trade-off between frequency resolution and variance.

5.2.2 Multitaper Estimator for the Bispectrum

We apply the theory developed by Brillinger for nth order cumulant spectra (Brillinger & Rosenblatt, 1967a, 1967b). The usual power spectrum is the 2nd-order cumulant spectrum we just presented above. In this paper, we also deal with the bispectrum, which is the 3rd-order cumulant spectrum, a function of the two frequencies (bifrequency) f_1 and f_2

$$B(f_1, f_2) = \mathrm{E}[X(f_1)X(f_2)X^*(f_1 + f_2)] \tag{4}$$

As mentioned above, the bispectrum has the favorable properties of zeroing Gaussian processes, being constant for linear systems with non-Gaussian input, and reflecting quadratic nonlinear interactions between bifrequency pairs f_1 and f_2 and their sum $f_1 + f_2$.

The Multitaper estimator for the bispectrum and bicoherence (Thomson, 1989; Birkelund et al., 2001)

$$\hat{B}_{k_1 k_2 k_3}(f_1, f_2) = X_{k_1,e}(f_1) X_{k_2,e}(f_2) X^*_{k_3,e}(f_1 + f_2) \tag{5}$$

$$\hat{B}(f_1, f_2) = \frac{1}{U_3} \sum_{k_1 k_2 k_3 = 0}^{K-1} P_{k_1 k_2 k_3} \hat{B}_{k_1 k_2 k_3}(f_1, f_2) \tag{6}$$

To preserve the correct scale, the 'bienergy' $P_{k_1 k_2 k_3} = \sum_{t=0}^{N_t - 1} v_{k_1}(t) v_{k_2}(t) v_{k_3}(t)$ and $U_3 = \frac{1}{N_t} \sum_{k_1, k_2, k_3}^{K} P^2_{k_1 k_2 k_3}$.

We estimate the bicoherence $b(f_1, f_2)$ using the following normalization of the bispectrum (Shahbazi et al., 2014), which benefits the statistical tests defined in the next section:

$$b(f_1, f_2) = \frac{B(f_1, f_2)}{\sqrt{S(f_1) S(f_2) S(f_1 + f_2)}} \tag{7}$$

5.2.3 Test for Gaussianity and linearity through Higher-Order Spectrum

To characterize the underlying dynamics of the time-series data, we employed higher-order spectral analysis to test for linearity and Gaussianity. Linear and nonlinear systems are fundamentally distinguished by their properties of response to input frequencies: a linear system processes frequencies independently, whereas a nonlinear system generates new harmonic and intermodulation components through frequency interactions. Bicoherence is utilized to detect and quantify this quadratic phase coupling.

The theoretical foundation for this method is predicated on the behavior of the bicoherence for a linear time-invariant (LTI) system. For an LTI system driven by a non-Gaussian input, the magnitude of the bicoherence, $|b(f_1, f_2)|$, is constant across all frequency pairs and is determined solely by the input signal's third-order (γ_3^x) and second-order (γ_2^x) cumulants (C. Nikias & Petropulu, 1993):

$$|b(f_1, f_2)| = \frac{|\gamma_3^x|}{(\gamma_2^x)^{3/2}}$$

This property yields a clear framework for hypothesis testing, details the result in Table 1:

1. A **Gaussian Linear (GL) process** is the null case. It has a third-order cumulant of zero, resulting in a bicoherence that is identically zero across all frequencies.
2. A **Non-Gaussian Linear (NGL) process** is driven by a non-Gaussian input passing through a linear system. This results in a **diffuse, widespread elevation** of bicoherence across the entire frequency plane.
3. A **Gaussian Nonlinear (GNL) process** involves a Gaussian input passing through a nonlinear system. The nonlinearity generates phase coupling at specific frequency interactions, producing **sharp, localized peaks** in the bicoherence plot against a near-zero background.
4. A **Non-Gaussian Nonlinear (NGNL) process** represents the combined case where a non-Gaussian input drives a nonlinear system. Its bicoherence exhibits both localized peaks superimposed on a diffuse, non-zero background.

To achieve a more nuanced understanding of underlying dynamics and explicitly separate system nonlinearity from input non-Gaussianity, this refined framework tries to detail the nonlinear case to GNL and NGNL. The test for intrinsic non-Gaussian input assesses the diffuse, central tendency of bicoherence, whereas the test for system nonlinearity targets sparse, high-magnitude peaks indicative of quadratic phase coupling. It is important to note that the term "non-Gaussian" within this framework refers to any deviation from Gaussianity in the observed time series that is not solely a result of system-induced phase coupling. This includes both non-Gaussian properties of the system's innovations (inputs) and the presence of independent additive non-Gaussian noise, both of which manifest as a diffuse, non-zero bicoherence.

The statistical implementation of these tests relies on the asymptotic distribution of the bispectrum estimator $\hat{B}(f_1, f_2)$. For a zero-mean stationary process, the bispectrum asymptotically follows the complex Gaussian distribution, its expected value and variance are given (Brillinger & Rosenblatt, 1967a)

$$\begin{aligned} \mathrm{E}\left[\hat{B}(f_1, f_2)\right] &= B(f_1, f_2) \\ \mathrm{Var}\left[\hat{B}(f_1, f_2)\right] &= S(f_1)S(f_2)S(f_1 + f_2) \end{aligned} \tag{8}$$

Statistical tests for (quadratic) Gaussianity and linearity can be effectively formulated using bicoherence, which measures quadratic phase coupling. The traditional test proposed by (Hinich, 1982) relies on the sum of squared bicoherence values, comparing the result to a chi-squared distribution. However, this sum-based approach is overly sensitive to extreme values, which can arise from strong, localized nonlinear interactions like narrow-band phase coupling. This sensitivity can cause the test to reject the null hypothesis of Gaussianity even when the process only exhibits isolated nonlinearity, leading to false positives. The sum is easily dominated by a few large values, misrepresenting the overall distribution as non-Gaussian.

For testing linearity specifically, traditional methods like the interquartile range (IQR) test are often inadequate. The IQR focuses on the central 50% of the bicoherence distribution, making it a poor detector of narrow-band quadratic phase coupling. Such interactions manifest as sparse, extreme values in the bicoherence map, which have little impact on the IQR. Consequently, the test lacks the power to identify significant but isolated nonlinear peaks.

To address these limitations, we propose two robust tests that enhance the Hinich framework by targeting distinct aspects of deviation from the null hypothesis. The first is a median-based test to assess central tendency for Gaussianity, and the second is a maximum-based test to detect nonlinear interactions. Both tests leverage bicoherence's ability to measure phase coupling, with their statistical properties validated through the theoretical derivations below.

5.2.3.1 Median-Based Test for Gaussianity

To provide a robust assessment of Gaussianity that is less affected by outliers, we introduce a test focused on the median of the squared bicoherence values. We first define a normalized statistic, $b^{(G)}$, which represents the median bicoherence magnitude and serves as a measure of effect size for asymmetricity:

$$b^{(G)} = \sqrt{\underset{f_1, f_2}{\text{median}}\{|b\,(f_1, f_2)|^2\}}$$

The formal test statistic, $t^{(G)}$, is a scaled version of this quantity:

$$t^{(G)} = 2N_s^{\text{eff}} \cdot (b^{(G)})^2 = 2N_s^{\text{eff}} \cdot \underset{f_1, f_2}{\text{median}}\{|b\,(f_1, f_2)|^2\}$$

where N_s^{eff} is the effective number of segments, and the median is computed over all bifrequency pairs (f_1, f_2). Under the null hypothesis of Gaussianity and linearity, this statistic follows an asymptotic normal distribution. The test evaluates:

$$P\{t^{(G)} > c_\alpha^{(G)}\} \approx \alpha \tag{9}$$

where $c_\alpha^{(G)}$ is the critical value from the asymptotic normal distribution at the significance level α. This test excels at detecting non-Gaussianity.

This test is derived from the asymptotical normal distribution of bicoherence. Under the null hypothesis of Gaussianity, for each independent bifrequency pair, the scaled squared bicoherence $x = 2N_s^{\text{eff}}|b(f_1, f_2)|^2$ follows a chi-squared distribution with two degrees of freedom $x \sim \chi^2(2)$. The test statistic $t^{(G)}$ is the sample median of P such independent variables. For a large number of bifrequency pairs P, the sample median is asymptotically normal. The population median of a $\chi^2(2)$ distribution is $m = 2\ln 2 \approx 1.386$. This is the expected value of our test statistic, $E[t^{(G)}] \approx 2\ln 2$. The asymptotic variance of a sample median from a sample of size P is given by $\frac{1}{4P[f(m)]^2}$, where $f(m)$ is the value of the probability density function (PDF) at the population median m. The PDF of a $\chi^2(2)$ distribution is $f(x) = \frac{1}{2}e^{-x/2}$. At the median $m = 2\ln 2$, the PDF value is $f(2\ln 2) = \frac{1}{2}e^{-\ln 2} = 1/4$. Therefore, the variance is:

$$\mathrm{Var}(t^{(G)}) = \frac{1}{4P(1/4)^2} = \frac{4}{P}$$

Thus, the test statistics follow the asymptotic distribution:

$$t^{(G)} \sim \mathcal{N}\left(2\ln 2, \sqrt{\frac{4}{P}}\right)$$

5.2.3.2 Maximum-Based Test for Nonlinearity

To identify nonlinear interactions that may be missed by the median test, we introduce a test based on the maximum squared bicoherence value. The normalized statistic, $b^{(L)}$, directly captures the magnitude of the strongest quadratic phase coupling:

$$b^{(L)} = \max_{f_1, f_2}\{|b\,(f_1, f_2)|\}$$

The corresponding test statistic, $t^{(L)}$, is its scaled squared value:

$$t^{(L)} = 2N_s^{\text{eff}} \cdot (b^{(L)})^{\,2} = 2N_s^{\text{eff}} \cdot \max_{f_1, f_2}\{|b\,(f_1, f_2)|^{\,2}\}$$

To distinguish localized linearity from background non-Gaussianity, we estimate a non-centrality parameter $\hat{\lambda}_0$. The distribution of $t^{(L)}$ is modeled using extreme value theory, specifically a Gumbel distribution. The test evaluates:

$$P\{t^{(L)} > c_\alpha^{(L)}\} \approx \alpha \tag{10}$$

where $c_\alpha^{(L)}$ is the critical value from the Gumbel distribution at the significance level α. This test is designed to pinpoint significant localized nonlinearity.

To account for baseline non-Gaussianity, we estimate a non-centrality parameter λ_0:

$$\hat{\lambda}_0 = \max\left(\operatorname*{median}_{f_1, f_2}\{2N_s^{\text{eff}}|b\,(f_1, f_2)|^{\,2}\} - 2\ln 2\,, 0\right)$$

This reflects that the median of a non-central $\chi^2(2, \lambda_0)$ distribution is approximately $2\ln 2 + \lambda_0$ for small λ_0. Using extreme value theory (EVT), the maximum of P independent $\chi^2(2, \lambda_0)$ variables is approximated by a Gumbel distribution. The normalizing constants are: $b_P = F^{-1}(1 - 1/P)$, the value where the cumulative distribution function (CDF) F of $\chi^2(2, \lambda_0)$ reaches $1 - 1/P$. And $a_P = \dfrac{1}{Pf(b_P)}$, where f is the PDF of $\chi^2(2, \lambda_0)$. Thus, the nonlinearity test statistic is distributed as:

$$t^{(L)} \sim \text{Gumbel}(b_P, a_P)$$

5.2.3.3 Estimation of the Effective Number of Segments

The theoretical distributions described above assume that bicoherence values are derived from independent data segments. However, modern spectral estimation techniques like the multitaper method we used here and the use of overlapping segments introduce dependencies. This means the nominal number of segments, N_s, is larger than the effective number of independent segments, N_s^{eff}. Using the nominal N_s in the test statistics will lead to incorrect scaling, thresholds, and p-values.

To ensure accuracy, we estimate N_s^{eff} with the following procedure:

1. Fit an AR model: Fit an autoregressive (AR) model to the observed time series $x(t)$ using the Burg method. Select the optimal model order using a criterion, here we use the Corrected Akaike Information Criterion (AICc).

2. Generate surrogate data: Generate M surrogate time series (e.g., $M = 100$) using the fitted AR model with Gaussian white noise as innovations. Each series should have the same length N as the original data.

3. Compute bicoherence: For each of the M surrogate series, compute the bicoherence $b(f_1, f_2)$ using the exact same parameters (e.g., multitaper settings, window length, overlap) as used for the original data.

4. Calculate the mean squared bicoherence: For each surrogate series, calculate the mean of the squared bicoherence magnitudes over all P valid bifrequency pairs:

$$\text{mean}(|b(f_1, f_2)|^2) = \frac{1}{P} \sum_{f_1, f_2} |b(f_1, f_2)|^2$$

5.Estimate N_s^{eff}: Average the result from step 4 across all M simulations. Under the null hypothesis, $E[|b(f_1, f_2)|^2] \approx 1/N_s^{\text{eff}}$. Therefore, the effective number of segments can be estimated as:

$$N_s^{\text{eff}} = \frac{1}{\text{mean}_M[\text{mean}(|b(f_1, f_2)|^2)]}$$

This estimated N_s^{eff} should replace N_s in all calculations for the $t^{(G)}$ and test statistics and their corresponding distributions, thereby accounting for dependencies and ensuring the validity of the statistical tests.

5.2.4 BiSpectral EEG Component Analysis (BiSCA)

5.2.4.1 Whole model

After obtaining the empirical and higher-order spectra, this paper proposed a BiSCA model specifically designed to detect nonlinear resonance by jointly parametrizing the spectrum and bispectrum. This combined model approach is essential for identifying nonlinear resonance phenomena that cannot be

detected by traditional spectral analysis alone. Here, the Xi trend and Rho peaks (including Alpha and all other oscillatory peaks) are modeled with two types of independent processes, allowing them to be additive on the natural scale. Additionally, the analysis includes both the spectrum and the bispectrum to understand the components comprehensively.

$$S(f;\theta_{2,\xi},\theta_{2,\rho}) = S_{\xi}(f;\theta_{2,\xi}) + S_{\rho}(f;\theta_{2,\rho}) \tag{11}$$

$$B(f_1,f_2;\theta_3) = B_{\xi}(f_1,f_2;\theta_{3,\xi}) + B_{\rho}(f_1,f_2;\theta_{3,\rho}) \tag{12}$$

where different θ are the parameters for different components in each order.

5.2.4.2 Model for Spectrum

In this paper, we put all peaks in the group of Rho processes for several reasons. 1) To be consistent with the conventional XiAlpha model, we model the trend as the Xi process and the oscillatory rhythms as the Alpha process. 2) The models of oscillation peaks have similar structures. 3) We focus on univariate analysis, which views the neural masses as a single integrated oscillator. For the spectra, each component consists of a sum of squares of kernel functions. Since here we use the transfer function to connect different orders of spectra, the sum of the squares of the frequency transfer function of each component approximates the modeled theoretical power spectra here

$$\begin{aligned} S_{\xi}(f;\sigma_{\xi},\nu_{\xi},d_{\xi}) &= h_{S,\xi}\, t(f;0,\sigma_{\xi},\nu_{\xi},d_{\xi})^{2} \\ S_{\rho}(f;\mu_{\rho},\sigma_{\rho},\nu_{\rho},d_{\rho}) &= \sum_{k=1}^{K} h_{S,\rho,k}\, t(f;\mu_{\rho},\sigma_{\rho},\nu_{\rho},d_{\rho})^{2} \end{aligned} \tag{13}$$

The kernel function $t(\cdot)$ models the oscillatory rhythm peaks in the spectrum domain. The h is the scale parameter for each peak, and the peak number K represents the number of harmonics to be modeled. We offered two strategies for determining the center frequency of peaks: (1) the $\{\mu_{\rho,k}\}$ is $\left\{\cdots,\frac{1}{3}\mu_{\alpha},\frac{1}{2}\mu_{\alpha},\mu_{\alpha},2\mu_{\alpha},3\mu_{\alpha},\cdots\right\}$, in practice, the order k is chosen with the Akaike information criteria. This circumstance models the alpha rhythm with the simplest condition that the resting state EEG is the output of the system excited with Gaussian white innovation, and the 1st-order transfer function has a single tone at Alpha; the rest of the peaks in other bands are the harmonics of the fundamental oscillation peak. (2) fit each of the $\{\mu_{\alpha,k}\}$ through the spectra and then adjust with the joint fitting with the bispectrum. Option (1) offers frequency peak organization following the

conventional broadband analysis; option (2) will fit the components better but is more complicated. This paper demonstrates the result with option (2), which is more general and can use the parameter for bicoherence to interpolate the phase relationship between the peaks. The goodness of both option fit is shown in the appendix.

The student t kernel function has been used in previous studies of spectrum fitting (Pascual-marqui et al., 1988; Newville et al., 2014; Haley & Anitescu, 2017). Here, we modified the student t function to model the amplitude of the 1st-order frequency transfer function, which also extends the adjustable heavy-tail version of the Lorentzian (Cauchy-Lorentz distribution function).

$$t(f,\mu,\sigma,\nu,d)=\frac{1}{\left[1+\left(\frac{f-\mu}{\sigma}\right)^{d}\right]^{\nu}} \tag{14}$$

The parameter σ controls the width of the kernel function. The parameter d controls the flat top of the kernel since the Multitaper method is smooth in the frequency domain and distorts the shape function; in practice, the value is larger than 2. The parameter ν controls the kurtosis or the heavy tail of the peak. Special case: $d=2$ it turns to the student t function; $\upsilon=1$, $d=2$ it turns to the Lorentzian kernel.

5.2.4.3 Model for bispectrum

To simplify the modeling process, we did not directly use the theoretical composition form of transfer function kernels to each order of the spectrum (Marzocca et al., 2008; Nichols et al., 2009; Billings, 2013; Peng et al., 2013; Jing & Lang, 2015). Instead, we focus on capturing the primary relationships of position and order by parameterizing the theoretical bispectrum $M_3(f_1,f_2)$ as follows:

$$\begin{aligned}\mathrm{Re}[M_3(f_1,f_2)]&=\mathrm{Re}(h_{B,\xi})t_2(f_1,f_2;\mu_\xi,\mu_\xi,\sigma_\xi,\nu_\xi,d_\xi) && \text{‘}\xi\text{’}\\ &+\sum_{m=1}^{K}\sum_{n=1}^{m}\mathrm{Re}(h_{B,\rho,m,n})t_2(f_1,f_2;\mu_{\rho,m},\mu_{\rho,n},\sigma_\rho,\nu_\rho,d_\rho) && \text{‘}\rho\text{’}\\ \mathrm{Im}[M_3(f_1,f_2)]&=\mathrm{Im}(h_{B,\xi})t_2(f_1,f_2;\mu_\xi,\mu_\xi,\sigma_\xi,\nu_\xi,d_\xi)\\ &+\sum_{m=1}^{K}\sum_{n=1}^{m}\mathrm{Im}(h_{B,\rho,m,n})t_2(f_1,f_2;\mu_{\rho,m},\mu_{\rho,n},\sigma_\rho,\nu_\rho,d_\rho)\end{aligned} \tag{15}$$

This formula captures the essential features of the bispectral peaks without resorting to complex transfer function compositions. The BiSCA models the real and imaginary parts of the bispectrum

separately since the phase information of the bispectrum is necessary for discrimination of systems (C. L. Nikias & Mendel, 1993). The kernel function for the bispectrum is

$$t_2(f_1,f_2;\mu_1,\mu_2,\sigma,\nu,d)=\frac{1}{t(f_1;\mu_1,\sigma,\nu,d)t(f_2;\mu_2,\sigma,\nu,d)t(f_1+f_2;\mu_1+\mu_2,\sigma,\nu,d)}$$

5.2.4.4 Likelihood

The likelihood of the model follows the asymptotically Gaussian distribution of the log-scale spectrum (Bevan et al., 1979) and natural scale bispectrum(Brillinger, 1985).

To ensure that the Xi process exhibits a wide spectrum, we add a likelihood term for the Xi process to encourage fits that adhere to the overall trend. The joint likelihood for the full model is:

$$\begin{aligned}L\left(\theta_2,\theta_3|\hat{S},\hat{B}\right)&=L\left(\theta_2|\tilde{S}\right)+L\left(\theta_3|\tilde{B}\right)\\&=-\frac{1}{N_S}\sum_f\left(\frac{\log\left(\hat{S}(f)\right)-\log\left(\tilde{S}(f;\theta_2)\right)}{\widehat{Var}\left[\log\left(\hat{S}(f)\right)\right]}\right)^2\\&-\frac{1}{N_B}\sum_{f_1}\sum_{f_2}\frac{\left|\hat{B}(f_1,f_2)-\tilde{B}(f_1,f_2;\theta_3)\right|^2}{\tilde{S}(f_1;\theta_2)\tilde{S}(f_2;\theta_2)\tilde{S}(f_1+f_2;\theta_2)}\end{aligned}$$

where the $\hat{S}(f)$ and $\hat{B}(f_1,f_2)$ is the Multitaper power spectrum and bispectrum estimate by formula (3) and **Error! Reference source not found.**, $\tilde{S}(f;\theta_2)$ and $\tilde{B}(f_1,f_2;\theta_3)$ is the modeled theoretical power spectrum and bispectrum.

This likelihood-based method makes it advantageous to use statistical methods to do the model comparison.

5.2.4.5 Fit with the Levenberg-Marquardt method

We estimate the model parameters using the Levenberg-Marquardt (LM) optimization algorithm. The LM method is a standard t echnique for solving nonlinear least squares problems, effectively balancing the Gauss-Newton algorithm and gradient descent. It is particularly suitable when the objective function is the sum of squares of loss functions, as in our joint likelihood estimation, which is also a heteroscedastic curve/surface fitting problem. Employing the LM method, we iteratively update the parameter estimates to minimize the discrepancy between the empirical and theoretical spectrum and

bispectrum, ensuring convergence to an optimal solution. The LM algorithm is not a global optimization method. Therefore, we fit the spectra parameters first and then share the parameters with the bispectrum as a warmup for the joint fit.

5.2.4.6 Bicoherence for each component

We can then obtain the bicoherence for each component

$$\tilde{b}_{\xi}(f_1, f_2) = \frac{\tilde{B}_{\xi}(f_1, f_2)}{\sqrt{S(f_1)S(f_2)S(f_1+f_2)}}$$

$$\tilde{b}_{\rho}(f_1, f_2) = \frac{\tilde{B}_{\rho}(f_1, f_2)}{\sqrt{S(f_1)S(f_2)S(f_1+f_2)}}$$

To avoid instability during fitting, we use full variance to normalize.

We use full variance to normalize the component bicoherence to avoid instability and ensure the additive way to model the bicoherence.

5.2.4.7 Test for components

Then we recall the test **Error! Reference source not found.** and **Error! Reference source not found.** for testing the non-Gaussianity and linearity of each component.

6. Data availability

The scalp EEG and intracranial EEG (iEEG) data analyzed in this study were obtained from the work of Li et al., (2022) and Frauscher et al. (2018), respectively.

7. Code availability

The analysis code used in this study will be made publicly available in a GitHub repository upon formal publication of this article, and the link will be provided.

8. References

Anh, V. V., Leonenko, N. N., & Sakhno, L. M. (2004). On a class of minimum contrast estimators for fractional stochastic processes and fields. *Journal of Statistical Planning and Inference*, *123*(1), 161–185. https://doi.org/10.1016/S0378-3758(03)00136-8

Anh, V. V., Leonenko, N. N., & Sakhno, L. M. (2007a). Minimum contrast estimation of random processes based on information of second and third orders. *Journal of Statistical Planning and Inference*, *137*(4), 1302–1331. https://doi.org/10.1016/j.jspi.2006.03.001

Anh, V. V., Leonenko, N. N., & Sakhno, L. M. (2007b). Statistical inference using higher-order information. *Journal of Multivariate Analysis*, *98*(4), 706–742. https://doi.org/10.1016/j.jmva.2006.09.009

Barry, R. J., & Blasio, F. M. D. (2021). Characterizing pink and white noise in the human electroencephalogram. *Journal of Neural Engineering*, *18*(3), 034001. https://doi.org/10.1088/1741-2552/abe399

Bartz, S., Avarvand, F. S., Leicht, G., & Nolte, G. (2019). Analyzing the waveshape of brain oscillations with bicoherence. *NeuroImage*, *188*, 145–160. https://doi.org/10.1016/j.neuroimage.2018.11.045

Bédard, C., Kröger, H., & Destexhe, A. (2006). Does the $1/f$ Frequency Scaling of Brain Signals Reflect Self-Organized Critical States? *Physical Review Letters*, *97*(11), 118102. https://doi.org/10.1103/PhysRevLett.97.118102

Bender, A., Voytek, B., & Schaworonkow, N. (2025). Resting-state alpha and mu rhythms change shape across development but lack diagnostic sensitivity for ADHD and autism. *Biorxiv*, 2023.10.13.562301. https://doi.org/10.1101/2023.10.13.562301

Bevan S., Kullberg R., & Rice J. (1979). An Analysis of Cell Membrane Noise. *The Annals of Statistics*, *7*(2), 237–257. https://doi.org/10.1214/aos/1176344609

Billings, S. A. (2013). *Nonlinear System Identification: NARMAX Methods in the Time, Frequency, and Spatio-Temporal Domains* (1st ed.). Wiley. http://gen.lib.rus.ec/book/index.php?md5=66b2821a252e489f0230a0ba4cb511aa

Birkelund, Y., Hanssen, A., & Powers, E. J. (2001). Multitaper estimation of bicoherence. *2001 IEEE International Conference on Acoustics, Speech, and Signal Processing. Proceedings (Cat. No.01CH37221)*, *5*, 3085–3088 vol.5. https://doi.org/10.1109/ICASSP.2001.940310

Bloniasz, P. F., Oyama, S., & Stephen, E. P. (2024). *Filtered point processes tractably capture rhythmic and broadband power spectral structure in neural electrophysiological recordings*. Cold Spring Harbor Laboratory. https://doi.org/10.1101/2024.10.01.616132

Brake, N., Duc, F., Rokos, A., Arseneau, F., Shahiri, S., Khadra, A., & Plourde, G. (2024a). A neurophysiological basis for aperiodic EEG and the background spectral trend. *Nature Communications*, *15*(1), 1514. https://doi.org/10.1038/s41467-024-45922-8

Brake, N., Duc, F., Rokos, A., Arseneau, F., Shahiri, S., Khadra, A., & Plourde, G. (2024b). A neurophysiological basis for aperiodic EEG and the background spectral trend. *Nature Communications*, *15*(1). https://doi.org/10.1038/s41467-024-45922-8

Breakspear, M. (2017). Dynamic models of large-scale brain activity. *Nature Neuroscience*, *20*(3), 340–352. https://doi.org/10.1038/nn.4497

Brillinger, D. R. (1985). FOURIER INFERENCE: SOME METHODS FOR THE ANALYSIS OF ARRAY AND NONGAUSSIAN SERIES DATA. *Journal of the American Water Resources Association*, *21*(5), 743–756. https://doi.org/10.1111/j.1752-1688.1985.tb00169.x

Brillinger, D. R. (2001). *Time Series: Data Analysis and Theory*. SIAM: Society for Industrial and Applied Mathematics. http://gen.lib.rus.ec/book/index.php?md5=183bc94159ab7babf5361702f7d9262d

Brillinger, D. R., & Rosenblatt, M. (1967a). ASYMPTOTIC THEORY OF ESTIMATES OF kTH-ORDER SPECTRA*. *Proceedings of the National Academy of Sciences*, *57*(2), 206–210. https://doi.org/10.1073/pnas.57.2.206

Brillinger, D. R., & Rosenblatt, M. (1967b). *Computation and interpretation of k-th order spectra*. https://www.stat.berkeley.edu/~brill/Papers/1967Computation.pdf

Carlqvist, H., Nikulin, V. V., Strömberg, J. O., & Brismar, T. (2005). Amplitude and phase relationship between alpha and beta oscillations in the human electroencephalogram. *Medical & Biological Engineering & Computing*, *43*(5), 599–607. https://doi.org/10.1007/BF02351033

Cole, S. R., van der Meij, R., Peterson, E. J., de Hemptinne, C., Starr, P. A., & Voytek, B. (2017). Nonsinusoidal beta oscillations reflect cortical pathophysiology in parkinson's disease. *The Journal of*

Neuroscience: The Official Journal of the Society for Neuroscience, *37*(18), 4830–4840. https://doi.org/10.1523/JNEUROSCI.2208-16.2017

Cole, S. R., & Voytek, B. (2017). Brain Oscillations and the Importance of Waveform Shape. *Trends in Cognitive Sciences*, *21*(2), 137–149. https://doi.org/10.1016/j.tics.2016.12.008

Cole, S., & Voytek, B. (2019). Cycle-by-cycle analysis of neural oscillations. *Journal of Neurophysiology*. https://doi.org/10.1152/jn.00273.2019

Connor, C. W. (2022). Signal, not noise: Aperiodic dynamics in the electroencephalogram under anesthesia. *Anesthesia and Analgesia*, 10.1213/ANE.7577. https://doi.org/10.1213/ANE.0000000000007577

Donoghue, T., Haller, M., Peterson, E. J., Varma, P., Sebastian, P., Gao, R., Noto, T., Lara, A. H., Wallis, J. D., Knight, R. T., Shestyuk, A., & Voytek, B. (2020). Parameterizing neural power spectra into periodic and aperiodic components. *Nature Neuroscience*, *23*(12), Article 12. https://doi.org/10.1038/s41593-020-00744-x

Donoghue, T., Schaworonkow, N., & Voytek, B. (2022). Methodological considerations for studying neural oscillations. *European Journal of Neuroscience*, *55*(11–12), 3502–3527. https://doi.org/10.1111/ejn.15361

Dragovic, S. Z., Ostertag, J., Baumann, N., García, P. S., Kratzer, S., Schneider, G., Schwerin, S., Sleigh, J., & Kreuzer, M. (2022). Spectral Differences of Anesthetic Agents: Addressing Fundamental Problems With New Methods. *Anesthesia and Analgesia*, 10.1213/ANE.7530. https://doi.org/10.1213/ANE.0000000000007530

Evertz, R., Hicks, D. G., & Liley, D. T. J. (2022). Alpha blocking and 1/fβ spectral scaling in resting EEG can be accounted for by a sum of damped alpha band oscillatory processes. *PLOS Computational Biology*, *18*(4), e1010012. https://doi.org/10.1371/journal.pcbi.1010012

Frauscher, B., von Ellenrieder, N., Zelmann, R., Doležalová, I., Minotti, L., Olivier, A., Hall, J., Hoffmann, D., Nguyen, D. K., Kahane, P., Dubeau, F., & Gotman, J. (2018). Atlas of the normal intracranial electroencephalogram: Neurophysiological awake activity in different cortical areas. *Brain*, *141*(4), 1130–1144. https://doi.org/10.1093/brain/awy035

Freyer, F., Aquino, K., Robinson, P. A., Ritter, P., & Breakspear, M. (2009). Bistability and non-gaussian fluctuations in spontaneous cortical activity. *Journal of Neuroscience*, *29*(26), 8512–8524. https://doi.org/10.1523/JNEUROSCI.0754-09.2009

Freyer, F., Roberts, J. A., Becker, R., Robinson, P. A., Ritter, P., & Breakspear, M. (2011). Biophysical Mechanisms of Multistability in Resting-State Cortical Rhythms. *Journal of Neuroscience*, *31*(17), 6353–6361. https://doi.org/10.1523/JNEUROSCI.6693-10.2011

Freyer, F., Roberts, J. A., Ritter, P., & Breakspear, M. (2012). A Canonical Model of Multistability and Scale-Invariance in Biological Systems. *PLoS Computational Biology*, *8*(8), e1002634. https://doi.org/10.1371/journal.pcbi.1002634

Grimbert, F., & Faugeras, O. (2006). Bifurcation Analysis of Jansen's Neural Mass Model. *Neural Computation*, *18*(12), 3052–3068. https://doi.org/10.1162/neco.2006.18.12.3052

Guimarães, D. A. (2021). Segmented Regression via the Shape Language Modeling for Multi-Slope Path-Loss Modeling. *Anais Do XXXIX Simpósio Brasileiro de Telecomunicações e Processamento de Sinais*. XXXIX Simpósio Brasileiro de Telecomunicações e Processamento de Sinais. https://doi.org/10.14209/sbrt.2021.1570730012

Haley, C. L., & Anitescu, M. (2017). Optimal bandwidth for multitaper spectrum estimation. *IEEE Signal Processing Letters*, *24*(11), 1696–1700. https://doi.org/10.1109/LSP.2017.2719943

He, H., & Thomson, D. J. (2010). Canonical bicoherence analysis of dynamic EEG data. *Journal of Computational Neuroscience*, *29*(1), 23–34. https://doi.org/10.1007/s10827-009-0177-z

Hinich, M. J. (1982). Testing for Gaussianity and Linearity of a Stationary Time Series. *Journal of Time Series Analysis*, *3*(3), 169–176. https://doi.org/10.1111/j.1467-9892.1982.tb00339.x

Hosking, J. R. M., & Wallis, J. R. (1997). *Regional Frequency Analysis: An Approach Based on L-Moments*. Cambridge University Press. https://doi.org/10.1017/CBO9780511529443

Hu, S., Zhang, Z., Zhang, X., Wu, X., & Valdes-Sosa, P. A. (2024). \bm\xi-\bm\pi: A nonparametric model for neural power spectra decomposition. *IEEE Journal of Biomedical and Health Informatics*, *28*(5), 2624–2635. https://doi.org/10.1109/JBHI.2024.3364499

Hughes, A. M., Whitten, T. A., Caplan, J. B., & Dickson, C. T. (2012). BOSC: A better oscillation detection method, extracts both sustained and transient rhythms from rat hippocampal recordings. *Hippocampus*, *22*(6), 1417–1428. https://doi.org/10.1002/hipo.20979

Idaji, M. J., Zhang, J., Stephani, T., Nolte, G., Müller, K.-R., Villringer, A., & Nikulin, V. V. (2022). Harmoni: A method for eliminating spurious interactions due to the harmonic components in neuronal data. *NeuroImage*, *252*, 119053. https://doi.org/10.1016/j.neuroimage.2022.119053

Isaksson, A., Lagergren, K., & Wennberg, A. (1976). Visible and non-visible EEG changes demonstrated by spectral parameter analysis. *Electroencephalography and Clinical Neurophysiology*, *41*(3), 225–236. https://doi.org/10.1016/0013-4694(76)90116-4

Jing, X., & Lang, Z. (2015). *Frequency Domain Analysis and Design of Nonlinear Systems based on Volterra Series Expansion: A Parametric Characteristic Approach*. Springer International Publishing. https://doi.org/10.1007/978-3-319-12391-2

Jirsa, V., & Müller, V. (2013). Cross-frequency coupling in real and virtual brain networks. *Frontiers in Computational Neuroscience*, *7*. https://doi.org/10.3389/fncom.2013.00078

Klimesch, W. (2012). Alpha-band oscillations, attention, and controlled access to stored information. *Trends in Cognitive Sciences*, *16*(12), 606–617. https://doi.org/10.1016/j.tics.2012.10.007

Kosciessa, J. Q., Grandy, T. H., Garrett, D. D., & Werkle-Bergner, M. (2020). Single-trial characterization of neural rhythms: Potential and challenges. *NeuroImage*, *206*, 116331. https://doi.org/10.1016/j.neuroimage.2019.116331

Kramer, M. A., & Chu, C. J. (2024). A general, noise-driven mechanism for the 1/f-like behavior of neural field spectra. *Neural Computation*, *36*(8), 1643–1668. https://doi.org/10.1162/neco_a_01682

Labecki, M., Kus, R., Brzozowska, A., Stacewicz, T., Bhattacharya, B. S., & Suffczynski, P. (2016). Nonlinear Origin of SSVEP Spectra—A Combined Experimental and Modeling Study. *Frontiers in Computational Neuroscience*, *10*. https://doi.org/10.3389/fncom.2016.00129

Lackey, H. E., Sell, R. L., Nelson, G. L., Bryan, T. A., Lines, A. M., & Bryan, S. A. (2023). Practical guide to chemometric analysis of optical spectroscopic data. *Journal of Chemical Education*, *100*(7), 2608–2626. https://doi.org/10.1021/acs.jchemed.2c01112

Leonenko, N. N., Sikorskii, A. Y., & Terdik, G. (1998). *On spectral and bispectral estimator of the parameter of nongaussian data*. *6*(2), 159–182. https://doi.org/10.1515/rose.1998.6.2.159

Li, M., Wang, Y., Lopez-Naranjo, C., Reyes, R. C. G., Hamid, A. I. A., Evans, A. C., Savostyanov, A. N., Calzada-Reyes, A., Areces-Gonzalez, A., Villringer, A., Tobon-Quintero, C. A., Garcia-Agustin, D., Paz-Linares, D., Yao, D., Dong, L., Aubert-Vazquez, E., Reza, F., Omar, H., Abdullah, J. M., … Valdes-Sosa, P. A. (2022). Harmonized-Multinational qEEG Norms (HarMNqEEG). *NeuroImage*, 119190. https://doi.org/10.1016/j.neuroimage.2022.119190

Lindén, H., Pettersen, K. H., & Einevoll, G. T. (2010). Intrinsic dendritic filtering gives low-pass power spectra of local field potentials. *Journal of Computational Neuroscience*, *29*(3), 423–444. https://doi.org/10.1007/s10827-010-0245-4

Lopes da Silva, F. H., van Rotterdam, A., Barts, P., van Heusden, E., & Burr, W. (1976). Models of Neuronal Populations: The Basic Mechanisms of Rhythmicity. In M. A. Corner & D. F. Swaab (Eds.), *Progress in Brain Research* (Vol. 45, pp. 281–308). Elsevier. https://doi.org/10.1016/S0079-6123(08)60995-4

Marcuse, L. V., Fields, M. C., & Yoo, J. J. (2015). *Rowan's Primer of EEG* (2nd edition). Elsevier.

Marzocca, P., Nichols, J. M., Milanese, A., Seaver, M., & Trickey, S. (2008). Second-order spectra for quadratic nonlinear systems by Volterra functional series: Analytical description and numerical simulation. *Mechanical Systems and Signal Processing*, *22*, 1882–1895. https://doi.org/10.1016/j.ymssp.2008.02.002

McKeon, S. D., Perica, M. I., Parr, A. C., Calabro, F. J., Foran, W., Hetherington, H., Moon, C.-H., & Luna, B. (2024). Aperiodic EEG and 7T MRSI evidence for maturation of E/I balance supporting the development of working memory through adolescence. *Developmental Cognitive Neuroscience*, *66*, 101373. https://doi.org/10.1016/j.dcn.2024.101373

Mendoza-Halliday, D., Major, A. J., Lee, N., Lichtenfeld, M. J., Carlson, B., Mitchell, B., Meng, P. D., Xiong, Y. (Sophy), Westerberg, J. A., Jia, X., Johnston, K. D., Selvanayagam, J., Everling, S., Maier, A., Desimone, R., Miller, E. K., & Bastos, A. M. (2024). A ubiquitous spectrolaminar motif of local field potential power across the primate cortex. *Nature Neuroscience*, *27*(3), 547–560. https://doi.org/10.1038/s41593-023-01554-7

Mohsini, K. A., Farooq, O., Khan, Y. U., & Tripathi, M. (2017). Bispectral analysis of EEG during non-convulsive seizures. *2017 International Conference on Multimedia, Signal Processing and Communication Technologies (IMPACT)*, 209–213. https://doi.org/10.1109/MSPCT.2017.8364006

Narasimhan, S. V. (1989). Pole-zero spectral modeling of EEG. *Signal Processing*, *18*(1), 17–32. https://doi.org/10.1016/0165-1684(89)90059-5

Newville, M., Stensitzki, T., Allen, D. B., & Ingargiola, A. (2014). *LMFIT: Non-Linear Least-Square Minimization and Curve-Fitting for Python* (Version 0.8.0) [Computer software]. Zenodo. https://doi.org/10.5281/zenodo.11813

Nichols, J. M., Olson, C. C., Michalowicz, J. V., & Bucholtz, F. (2009). The Bispectrum and Bicoherence for Quadratically Nonlinear Systems Subject to Non-Gaussian Inputs. *IEEE Transactions on Signal Processing*, *57*(10), 3879–3890. IEEE Transactions on Signal Processing. https://doi.org/10.1109/TSP.2009.2024267

Nikias, C. L., & Mendel, J. M. (1993). Signal processing with higher-order spectra. *IEEE Signal Processing Magazine*, *10*(3), 10–37. https://doi.org/10.1109/79.221324

Nikias, C., & Petropulu, A. (1993). *Higher Order Spectra Analysis: A Non-Linear Signal Processing Framework* (Facsimile edition). Pearson.

Nozari, E., Bertolero, M. A., Stiso, J., Caciagli, L., Cornblath, E. J., He, X., Mahadevan, A. S., Pappas, G. J., & Bassett, D. S. (2024). Macroscopic resting-state brain dynamics are best described by linear models. *Nature Biomedical Engineering*, *8*(1), 68–84. https://doi.org/10.1038/s41551-023-01117-y

Pascual-Marqui, R. D., Kochi, K., & Kinoshita, T. (2022). *Cortical Xi-Alpha model for resting state electric neuronal activity* (No. arXiv:2212.13571). arXiv. https://doi.org/10.48550/arXiv.2212.13571

Pascual-marqui, R. D., Valdes-sosa, P. A., & Alvarez-amador, A. (1987). A Parametric Model for Multichannel EEG Spectra. *International Journal of Neuroscience*, *40*(1–2), 89–99. https://doi.org/10.3109/00207458808985730

Pascual-marqui, R. D., Valdes-sosa, P. A., & Alvarez-amador, A. (1988). A Parametric Model for Multichannel EEG Spectra. *International Journal of Neuroscience*, *40*(1–2), 89–99. https://doi.org/10.3109/00207458808985730

Peng, Z. K., Zhang, W. M., Yang, B. T., Meng, G., & Chu, F. L. (2013). The parametric characteristic of bispectrum for nonlinear systems subjected to Gaussian input. *Mechanical Systems and Signal Processing*, *36*(2), 456–470. https://doi.org/10.1016/j.ymssp.2012.10.010

Pfanzagl, J. (1969). On the measurability and consistency of minimum contrast estimates. *Metrika*, *14*(1), 249–272. https://doi.org/10.1007/BF02613654

Price-Whelan, A. M., Lim, P. L., Earl, N., & Others. (2022). The Astropy Project: Sustaining and Growing a Community-oriented Open-source Project and the Latest Major Release (v5.0) of the Core Package. *Astrophys. J.*, *935*(2), 167. INSPIRE. https://doi.org/10.3847/1538-4357/ac7c74

Raffaelli, G. T., Jiříček, S., & Hlinka, J. (2024). *Nonlinear brain connectivity from neurons to networks: Quantification, sources and localization* (p. 2024.11.17.623635). bioRxiv. https://doi.org/10.1101/2024.11.17.623635

Reyes, R. G., Gonzales, A. A., Wang, Y., Jin, Y., Minatti, L., & Valdes-Sosa, P. A. (2025). *Lifespan mapping of EEG source spectral dynamics with ξ − αNET* (p. 2025.02.21.639413). bioRxiv. https://doi.org/10.1101/2025.02.21.639413

Rice, J. (1979). On the estimation of the parameters of a power spectrum. *Journal of Multivariate Analysis*, *9*(3), 378–392. https://doi.org/10.1016/0047-259X(79)90095-2

Riedel, K. S., & Sidorenko, A. (1995). Minimum bias multiple taper spectral estimation. *IEEE Transactions on Signal Processing*, *43*(1), 188–195. IEEE Transactions on Signal Processing. https://doi.org/10.1109/78.365298

Roberts, J. A., & Robinson, P. A. (2012). Quantitative theory of driven nonlinear brain dynamics. *NeuroImage*, *62*(3), 1947–1955. https://doi.org/10.1016/j.neuroimage.2012.05.054

Sakhno, L. (2014). Minimum Contrast Method for Parameter Estimation in the Spectral Domain. In V. Korolyuk, N. Limnios, Y. Mishura, L. Sakhno, & G. Shevchenko (Eds.), *Modern Stochastics and Applications* (pp. 319–336). Springer International Publishing. https://doi.org/10.1007/978-3-319-03512-3_18

Sakhno, L. (2020). On the Estimation of Spectral Functionals of the Fourth Order for Stationary Random Fields. *Austrian Journal of Statistics*, *49*(4), 106–116. https://doi.org/10.17713/ajs.v49i4.1136

Schaworonkow, N. (2023). Overcoming harmonic hurdles: Genuine beta-band rhythms vs. contributions of alpha-band waveform shape. *Imaging Neuroscience*, *1*, 1–8. https://doi.org/10.1162/imag_a_00018

Schaworonkow, N., & Nikulin, V. V. (2019). Spatial neuronal synchronization and the waveform of oscillations: Implications for EEG and MEG. *PLOS Computational Biology*, *15*(5), e1007055. https://doi.org/10.1371/journal.pcbi.1007055

Schaworonkow, N., & Nikulin, V. V. (2022). Is sensor space analysis good enough? Spatial patterns as a tool for assessing spatial mixing of EEG/MEG rhythms. *NeuroImage*, *253*, 119093. https://doi.org/10.1016/j.neuroimage.2022.119093

Seymour, R. A., Alexander, N., & Maguire, E. A. (2022). Robust estimation of 1/f activity improves oscillatory burst detection. *European Journal of Neuroscience*, *56*(10), 5836–5852. https://doi.org/10.1111/ejn.15829

Shahbazi Avarvand, F., Bartz, S., Andreou, C., Samek, W., Leicht, G., Mulert, C., Engel, A. K., & Nolte, G. (2018). Localizing bicoherence from EEG and MEG. *NeuroImage*, *174*(October 2017), 352–363. https://doi.org/10.1016/j.neuroimage.2018.01.044

Shahbazi, F., Ewald, A., & Nolte, G. (2014). Univariate normalization of bispectrum using Hölder's inequality. *Journal of Neuroscience Methods*, *233*, 177–186. https://doi.org/10.1016/j.jneumeth.2014.05.030

Silva, L. R., Amitai, Y., & Connors, B. W. (1991). Intrinsic oscillations of neocortex generated by layer 5 pyramidal neurons. *Science*, *251*(4992), 432–435. https://doi.org/10.1126/science.1824881

Spiegler, A., Kiebel, S. J., Atay, F. M., & Knösche, T. R. (2010). Bifurcation analysis of neural mass models: Impact of extrinsic inputs and dendritic time constants. *NeuroImage*, *52*(3), 1041–1058. https://doi.org/10.1016/j.neuroimage.2009.12.081

Stark, J., Broomhead, D. S., Davies, M. E., & Huke, J. (1997). Takens embedding theorems for forced and stochastic systems. *Nonlinear Analysis: Theory Methods & Applications*, *30*(8), 5303–5314. https://doi.org/10.1016/S0362-546X(96)00149-6

Stiefel, K. M., & Ermentrout, G. B. (2016). Neurons as oscillators. *Journal of Neurophysiology*, *116*(6), 2950–2960. https://doi.org/10.1152/jn.00525.2015

Takens, F. (1985). On the numerical determination of the dimension of an attractor. In B. L. J. Braaksma, H. W. Broer, & F. Takens (Eds.), *Dynamical Systems and Bifurcations* (Vol. 1125, pp. 99–106). Springer Berlin Heidelberg. https://doi.org/10.1007/BFb0075637

Thomson, D. J. (1982). Spectrum estimation and harmonic analysis. *Proceedings of the IEEE*, *70*(9), 1055–1096. Proceedings of the IEEE. https://doi.org/10.1109/PROC.1982.12433

Thomson, D. J. (1989). Multi-window Bispectrum Estimates. *Workshop on Higher-Order Spectral Analysis*, 19–23. https://doi.org/10.1109/HOSA.1989.735263

Travert, A., & Fernandez, C. (2024). *SpectroChemPy* (Version 0.6.9) [Computer software]. Zenodo. https://doi.org/10.5281/ZENODO.3823841

Valdes, P. A., Jimenez, J. C., Riera, J., Biscay, R., & Ozaki, T. (1999). Nonlinear EEG analysis based on a neural mass model. *Biological Cybernetics*, *81*(5–6), 415–424. https://doi.org/10.1007/s004220050572

Valdés, P., Bosch, J., Grave, R., Hernandez, J., Riera, J., Pascual, R., & Biscay, R. (1992). Frequency domain models of the EEG. *Brain Topography*, *4*(4), 309–319. https://doi.org/10.1007/BF01135568

Valdés-Sosa, P., Bosch, J., Jiménez, J., Trujillo-Barreto, N., Lirio, R. J., Morales, F., Hernandez Caceres, J. luis, & Ozaki, T. (1999). The statistical identification of nonlinear brain dynamics: A progress report. In *Non linear Dynamic and Brain Funcioning* (pp. 278–284).

Van Albada, S., & Robinson, P. (2013a). Relationships between Electroencephalographic Spectral Peaks Across Frequency Bands. *Frontiers in Human Neuroscience*, *7*. https://doi.org/10.3389/fnhum.2013.00056

Van Albada, S., & Robinson, P. (2013b). Relationships between Electroencephalographic Spectral Peaks Across Frequency Bands. *Frontiers in Human Neuroscience*, *7*. https://www.frontiersin.org/articles/10.3389/fnhum.2013.00056

Van Kerkoerle, T., Self, M. W., Dagnino, B., Gariel-Mathis, M.-A., Poort, J., Van Der Togt, C., & Roelfsema, P. R. (2014). Alpha and gamma oscillations characterize feedback and feedforward processing in monkey visual cortex. *Proceedings of the National Academy of Sciences*, *111*(40), 14332–14341. https://doi.org/10.1073/pnas.1402773111

Wang, Y., Li, M., Paz-Linares, D., Areces-Gonzalez, A., Bringas-Vega, M., Bosch-Bayard, J., & Valdes-Sosa, P. (2024). Group-level current source reconstruction of the MNI iEEG atlas. *The Organization for Human Brain Mapping (OHBM) 2024 Annual Meeting*, 1657. https://archive.aievolution.com/2024/hbm2401/Abstracts/viewAbs?abs=3058

Wang, Y., Li, M., Reyes, R. G., Ronaldo García Reyes, Bosch-Bayard, J., Bringas-Vega, M., Michael Breakspear, Minati, L., & Valdes-Sosa, P. (2025). Nonlinear properties of multistable states of intracranial EEG. *The Organization for Human Brain Mapping (OHBM) 2025 Annual Meeting*, 1339.

Wen, H., & Liu, Z. (2016). Separating Fractal and Oscillatory Components in the Power Spectrum of Neurophysiological Signal. *Brain Topography*, *29*(1), 13–26. https://doi.org/10.1007/s10548-015-0448-0

Wilson, L. E., da Silva Castanheira, J., & Baillet, S. (2022a). Time-resolved parameterization of aperiodic and periodic brain activity. *eLife*, *11*, e77348. https://doi.org/10.7554/eLife.77348

Wilson, L. E., da Silva Castanheira, J., & Baillet, S. (2022b). Time-resolved parameterization of aperiodic and periodic brain activity. *eLife*, *11*, e77348. https://doi.org/10.7554/eLife.77348

Zandvoort, C. S., & Nolte, G. (2021). Defining the filter parameters for phase-amplitude coupling from a bispectral point of view. *Journal of Neuroscience Methods*, *350*, 109032. https://doi.org/10.1016/j.jneumeth.2020.109032

Zetterberg, L. H. (1969). Estimation of parameters for a linear difference equation with application to EEG analysis. *Mathematical Biosciences*, *5*(3), 227–275. https://doi.org/10.1016/0025-5564(69)90044-3

Zetterberg, L. H., Kristiansson, L., & Mossberg, K. (1978). Performance of a model for a local neuron population. *Biological Cybernetics*, *31*(1), 15–26. https://doi.org/10.1007/BF00337367

Zhou, R., Yu, Y., & Li, C. (2024). Revealing neural dynamical structure of C. elegans with deep learning. *Iscience*, *27*(5). https://doi.org/10.1016/j.isci.2024.109759

Appendix

A.1 Mathematical notations

Table A 1 Basic mathematical symbols

Symbol	Definition
$x \in \mathbb{C}$ or $x \in \mathbb{C}$	Scalar
$\boldsymbol{x} \in \mathbb{C}^d$	Vector of size d (e.g., $\boldsymbol{x} = [x_i \vert i = 1, \cdots, d]$)
$\boldsymbol{X} \in \mathbb{C}^{d_1 \times d_2}$	Matrix of size $d_1 \times d_2$

Table A 2 Summary of indices

Symbol	Definition
i	Index of individual $i \in \{1, 2, \cdots N_i\}$, N_i is the total participants or subjects in the study
c	Index of the channel $c \in \{1, 2, \cdots, N_c\}$, N_c is total EEG channels
e	Index of EEG epochs $e \in \{1, 2, \cdots, N_e\}$, N_e is the disjoint segments selected from the continuous EEG
f	Physical frequencies with unit Hz
t	Physical time of each epoch
k	Index of taper, $k \in \{1, 2, \cdots, N_k\}$, where $N_k = 2NW - 1$
NW	Time-bandwidth product. N is the number of time samples in a single EEG epoch. W is the half-bandwidth of the tapers

Table A 3 Symbol of quantities and operators

Symbol	Name	Definition
$v_{i,c,e}(t) \in \mathbb{R}$ $v_{i,c,e}(f) \in \mathbb{C}$	EEG potential and its Discrete Fourier transform	EEG potential of the individual i, channel c of e -th epoch at a time t or frequency f for the Discrete Fourier transform.
$S_{i,c}(f) \in \mathbb{R}$	Theoretical spectra	The theoretical spectrum of an individual i channel c at the frequency f
$\hat{S}_{i,c}(f) \in \mathbb{R}$	Power spectra	The empirical variance vector of $v_{i,c,e}(f)$ across all epochs for an individual i at the frequency f
$B_{i,c}(f_1, f_2) \in \mathbb{C}$	Theoretical Bispectrum	The theoretical bispectrum of an individual channel c at the bifrequency (f_1, f_2)

$\hat{B}_{i,c}(f_1, f_2) \in \mathbb{C}$	Empirical Bispectrum	The empirical bispectrum of process $v_{i,c,e}(t)$ across all epochs for an individual i channel c at the bifrequency (f_1, f_2)
$b_{i,c}(f_1, f_2) \in \mathbb{C}$	Population Bicoherence	Population normalized bispectrum for individual i and channel c at the bifrequency (f_1, f_2)
$\hat{b}_{i,c}(f_1, f_2) \in \mathbb{C}$	Multitaper Bicoherence	Multitaper bicoherence estimator for individual i and channel c for bifrequency (f_1, f_2)
$\tilde{b}_{i,c}(f_1, f_2) \in \mathbb{C}$	BisCA Bicoherence	BiSCA -model estimator for individual i and channel c for bifrequency (f_1, f_2)
$\mathrm{E}[\cdot]$	Expectation	The expectation of a random variable
$\mathrm{Var}[\cdot]$	Variance	The variance of a random variable
$[\cdot]^*$	Complex conjugate	The complex conjugate of a variable

A.2 Summary of EEG Spectral Parameterization Methods

As a typical machine learning problem, many toolboxes implemented the curve fitting for spectroscopic data analysis - such as SpectroChemPy (Travert & Fernandez, 2024), PNNL Chemometric Toolbox(Lackey et al., 2023) astronomy data.modeling (Price-Whelan et al., 2022), SLM (Shape Language Modeling) (Guimarães, 2021), LMFIT (Levenberg-Marquardt least-squares minimization)(Newville et al., 2014). This paper emphasizes studies that have been applied specifically to EEG spectral analysis with certain constraints of biophysical prior.

Table A 4 Summary of EEG Spectral Parameterization Methods

Method	Feature	Citation
SPA (Spectral Parameter Analysis)	Calculate the resonance peaks information from the poles and zeros of the autoregressive model	(Zetterberg, 1969; Isaksson et al., 1976; Narasimhan, 1989)
Xi-Alpha (ξα)	Additive t-student kernels in nature scale fitted with maximum Whittle's likelihood	(Pascual-marqui et al., 1987)
BOSC (Better Oscillation Detection)	Thresholds for time and amplitude to detect and parametrize the burst of rhythm in time frequency	(Hughes et al., 2012; Kosciessa et al., 2020; Seymour et al., 2022)

Gaussian peak fit	Least square Gaussian peak fit	(Van Albada & Robinson, 2013b)
IRASA (Irregular-Resampling Auto-Spectral Analysis)	Resampling to shift the spectra and using a media curve to get components	(Wen & Liu 2016)
SpecParam (Spectral parameterization) or FOOOF (Fitting Oscillations & One Over F)	Sequentially fit peaks through least square Gaussian fit in the log-scale	(Donoghue et al., 2020)
SPRiNT (Spectral Parameterization Resolved in Time)	Parametrize the peaks in the smoothed short-time Fourier transforms	(Wilson et al., 2022b)
PaWNextra (Pink and White Noise extraction)	Least square fit	(Barry & Blasio, 2021)
Cortical Xi-Alpha	Nonnegative matrix decomposition for multichannel	(Pascual-Marqui et al., 2022)
Xi-Pi (ξ-π)	Fit nonparametric spectrum components with Whittle's likelihood	(Hu et al., 2024)
Xi-Alpha Net	Hierarchical Bayesian model for solving the State space model with Xi-Alpha prior to reconstruct the source space spectrum	(Reyes et al., 2025)
BiSCA (Higher-order Xi-Alpha Model)	Parametrize both spectrum and bispectrum with joint likelihood	This paper

A.3 Simulation

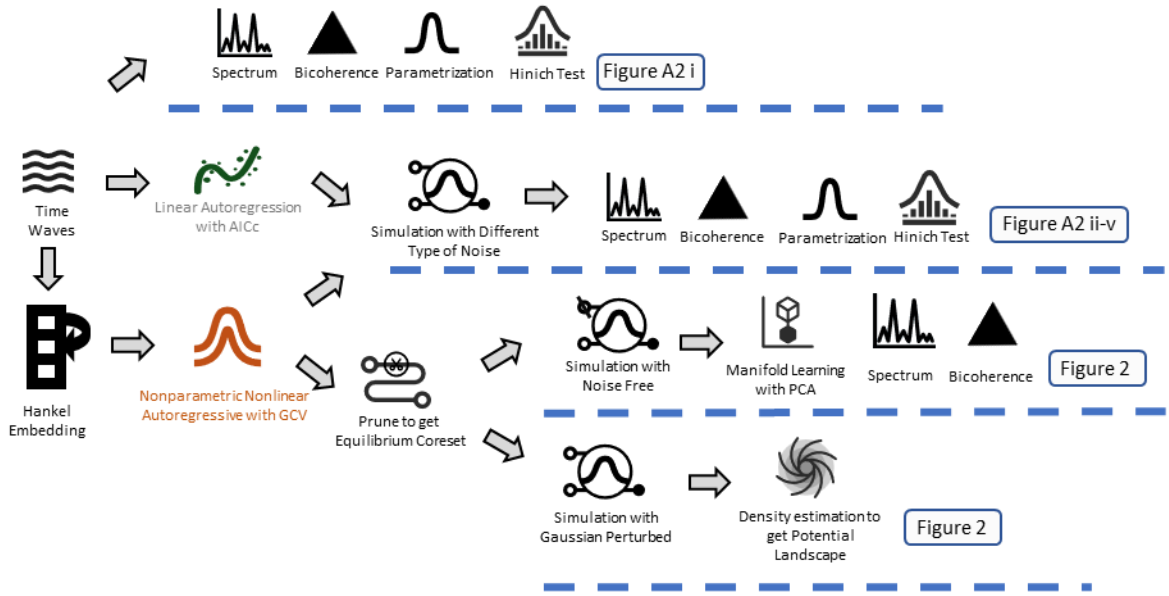

Figure A 1 Flowchart of the Simulation and Analysis Pipeline. *This diagram illustrates the methodology for analyzing real intracranial EEG (iEEG) data and generating four corresponding types of synthetic surrogate data to test for nonlinearity and non-Gaussianity, also the demonstration graph in Figure 2. (1) Direct Analysis of Real Data (Top Path, Ref: Figure A2 i): The process begins with a real iEEG time series. This signal is directly subjected to spectral and bispectral analysis to compute its empirical power spectrum and bicoherence, establishing a real-data baseline. (2) Linear and Nonlinear Surrogate Generation (Middle Path, Ref: Figure A2 ii-v): A linear Autoregressive (AR) and a Nonparametric Nonlinear Autoregressive (NNAR) model is fitted to the real iEEG data. The optimal model order is selected using the Akaike Information Criterion corrected (AICc). This AR model and NNAR model are then used to generate two types of time series by driving it with different stochastic innovations: Linear/Nonlinear Gaussian: Using Gaussian (normal) distributed noise. Linear/Nonlinear Non-Gaussian: Using skewed, non-Gaussian noise (Pearson Type III distribution). (3). Simulation demonstration of the bicoherence and time domain Geometric for the Figure 2: after fitting the NNAR model to the real data, only the states close to the equilibrium is be maintained in the model and used to simulate to get spectrum, bicoherence and 2d embedded potential (density) function.*

A.3.1 Simulation for the Hinich's test and BiSCA parametrization demonstration

Here is an example of our bicoherence analysis for different types of signals, we put a simulation demonstration consisting of one channel of real data and 4 corresponding synthetic data (linear Gaussian, linear non-gaussian, nonlinear Gaussian, and nonlinear non-gaussian).

1. Real data: one channel from the MNI atlas data, with Fs=200 and 12000 time points samples.
2. Linear Gaussian process: This simulation used an Autoregressive (AR) model with Gaussian innovation.

$$\tilde{x}_{t+1} = \sum_{i=0}^{p-1} \hat{a}_i \tilde{x}_{t-i} + \tilde{u}_t (t = p, ..., N + p - 1) \tag{16}$$

The AR coefficient is fitted with the real data using Burg's method. In this example, a 45-order AR model is selected with AICc criteria, and the innovation is $N(0,1)$. We simulated $N=12000$ samples with this AR model, also the same length for the rest 3 simulations.

3. Linear non-gaussian process: Instead of using the Gaussian innovation, here we use the Pearson type III distribution(Hosking & Wallis, 1997) as the innovation enables us to control the first to third-order moment for the distribution. The probability density function is

$$f(u)=\begin{cases}\dfrac{(u-\xi)^{\alpha-1}e^{-(u-\xi)/\beta}}{\beta^{\alpha}\Gamma(\alpha)}, & \gamma>0\\ \dfrac{1}{\sqrt{2\pi}}e^{-\frac{1}{2}\left(\frac{u-\mu}{\sigma}\right)^{2}}, & \gamma=0\\ \dfrac{(u-\xi)^{\alpha-1}e^{-(\xi-u)/\beta}}{\beta^{\alpha}\Gamma(\alpha)}, & \gamma<0\end{cases} \tag{17}$$

where the parameter of the distribution $\alpha=4/\gamma^2$, $\beta=\frac{1}{2}\sigma|\gamma|$ and $\xi=\mu-2\sigma/\gamma$. The parameter μ is the center of distribution, σ is the standard deviation, γ is the skewness. Here we take $\mu=0$, $\sigma=1$ and $\gamma=10$.

4. Nonlinear Gaussian process: Instead of linear p-lag AR model in the linear case, here we used a nonparametric nonlinear autoregressive (NNAR) model to fit the data (Valdés-Sosa et al., 1999), and simulate 12000 timepoints data recursively. Given timeseries $\{x_t\}_{t=1}^{N_t}$, reconstruct phase space via delay embedding:

$$\boldsymbol{x}_t=[x_t,x_{t-1},\ldots,x_{t-p+1}]^T\in\mathbb{R}^p \tag{18}$$

The state evolution is modeled as the discrete nonlinear state space model

$$\tilde{\boldsymbol{x}}_{t+1}=F(\tilde{\boldsymbol{x}}_t)+\tilde{\boldsymbol{u}}_t \tag{19}$$

where $F(\cdot):\mathbb{R}^p\to\mathbb{R}^p$ is a p dimensional nonparametric function estimated via adaptive local constant regression (Nadaraya-Waston regression). To simplify the notation to fit regression notation, define embedding vector keys set $\{\boldsymbol{x}_k,\boldsymbol{y}_k\}_{k=1}^{n}$ stored all observed data with $\boldsymbol{x}_k=\boldsymbol{x}_t$ and $\boldsymbol{y}_k=\boldsymbol{x}_{t+1}$, $n=N_t-p-1$.

$$\hat{F}(\boldsymbol{x}_q^*) = \frac{\sum_{k=1}^{n} K_{h_k}(\boldsymbol{x}_k, \tilde{\boldsymbol{x}}_q)\boldsymbol{y}_k}{\sum_{k=1}^{n} K_{h_k}(\boldsymbol{x}_k, \tilde{\boldsymbol{x}}_q)} \tag{20}$$

$\tilde{\boldsymbol{x}}_q$ is the query vector state during the N-step forward forecasting. The local weights are calculated by the kernel distance $K_{h_k}(\boldsymbol{x}_k, \boldsymbol{x}_q) = \exp\left(-\frac{\| \boldsymbol{x}_k - \boldsymbol{x}_q \|^2}{2h_k^2}\right)$ with bandwidth h_k. The h_k is the hyper parameter of model, in order to handle non-uniform distribution of the states in the p dimension space, we use the κ-th nearest neighborhood $\boldsymbol{x}_{[k,\kappa]}$ of each $\boldsymbol{x}_k$ to determine the local bandwidth

$$h_k = \frac{\| \boldsymbol{x}_{[k,\kappa]} - \boldsymbol{x}_k \|}{\sqrt{p}} \tag{21}$$

To select κ, this paper used a generalized cross-validation (GCV) on the real data $\{x_t\}_{t=1}^{N}$ from case 1, to find the best κ of and record the corresponding h_k for each states $\boldsymbol{x}_k$ in the one-step forward prediction task.

$$\mathrm{GCV}(\kappa) = \frac{\mathrm{MSE}(\kappa)}{(1 - \mathrm{tr}(\boldsymbol{L}(\kappa))/n)^2}$$

where the smoother matrix with elements

$$L_{k,q}(\kappa) = \frac{K_{h_k}(\boldsymbol{x}_k, \boldsymbol{x}_q)}{\sum_{k=1}^{n-1} K_{h_k}(\boldsymbol{x}_k, \boldsymbol{x}_q)}$$

To be computationally efficient, here we use scalar h_k, bandwidth is equal for all dimensions. The embedding dimensions p are used the same as linear simulation case 2 and case 3. The nonparametric function $\hat{F}(\cdot)$ represent all the information of the original (Hankel embedded) state space or the differential manifold of the system, therefore, we didn't update this nonparametric function during evolution. In the simulation the innovation $\boldsymbol{u}_t^*$ is a multivariable gaussian distribution $\boldsymbol{z}_t$ and scaled with covariance from the residual of the one-step forward

prediction $\boldsymbol{u}_t^* = \boldsymbol{L}\boldsymbol{z}_t$, where $\boldsymbol{L}$ is the Cholesky of the covariance matrix of the residual $\boldsymbol{L}\boldsymbol{L}^T = \boldsymbol{\Sigma}$, and $\boldsymbol{\Sigma} = \frac{1}{n-1}\boldsymbol{\epsilon}^T\boldsymbol{\epsilon} + \lambda \boldsymbol{I}_p$ with $\boldsymbol{\epsilon} = \boldsymbol{X} - \hat{\boldsymbol{X}} = [\epsilon_{t,1}, \epsilon_{t,2}, \ldots, \epsilon_{t,p}]_{t=1}^n$.

5. Nonlinear non-gaussian process: The nonlinear system follows the configuration of case 4. Instead of Gaussian innovation, we use Pearson type III (17) to generate the innovation $\boldsymbol{z}_t$ and then the $\boldsymbol{u}_t^*$.

All 5 cases apply the Multitaper estimation and the BiSCA model fitting with the same parameters as the analysis for real data.

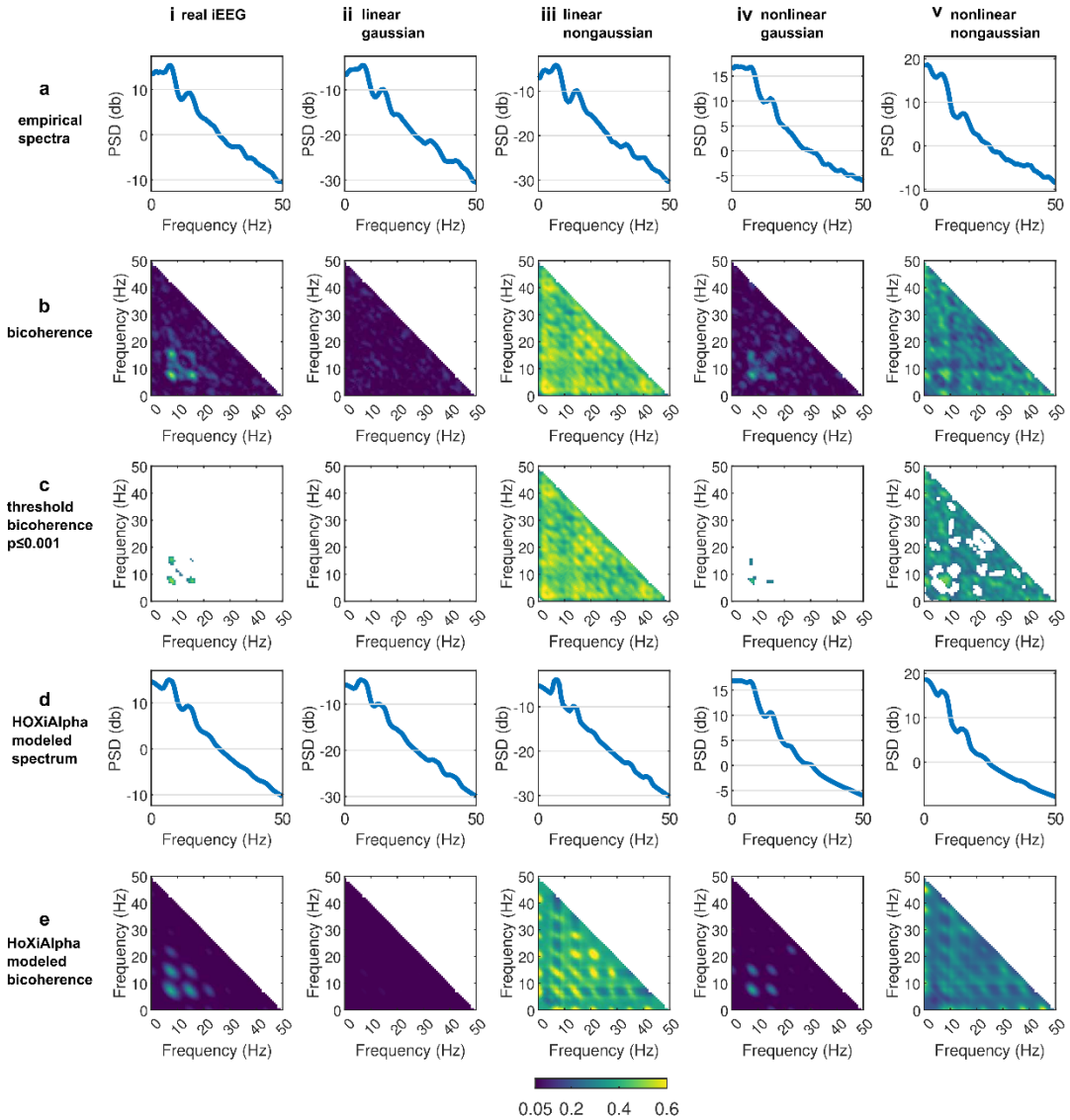

Figure A 2 Simulation demonstration. *Column from left to right are the 5 cases described in the simulation (i) real iEEG of MNI atlas data; (ii) linear Gaussian; (iii) linear non-Gaussian ; (iv) nonlinear Gaussian; (v) nonlinear non-Gaussian; Row from top to bottom is the result of analysis of each step (a) empirical spectrum calculated with Multitaper method; b) empirical modulus bicoherence calculated with Multitaper method with color scale indicating bicoherence modulus amplitude.; (c) threshold bicoherence with parametric test of p≤0.001: providing a clearer view of which frequency interactions are nonlinearly coupled beyond test level; (d) the spectrum from the fitted BiSCA model; (e) the bicoherence from the fitted BiSCA model: illustrating how well the model captures the observed nonlinear/non-Gaussian dynamics*

Figure A 2 illustrates how non-Gaussianity and nonlinearity impact neural time series analyses; we synthesized intracranial EEG (iEEG) signals under five distinct scenarios - real iEEG data (MNI atlas), linear Gaussian, linear non-Gaussian, nonlinear Gaussian, and nonlinear non-Gaussian - and compared their power spectrum and bicoherence pattern. The real iEEG data Figure A 2i exhibits a characteristic

1/f-like power spectrum with modest but significant bicoherence clusters after thresholding ($p \leq 0.001$). This empirical baseline reveals that genuine neural signals naturally contain nonlinear and Gaussian features.

In the Figure A 3 we show the result of statistic test of Figure A 2. Real iEEG (Top-Left): Both tests are significant, indicating the presence of both nonlinear interactions and non-Gaussian characteristics in the neural data. Linear Gaussian (Middle-Left): As expected for the null case, neither test is significant, correctly identifying the signal as linear and Gaussian. Linear Non-Gaussian (Middle-Right): Only the Gaussian test is significant, demonstrating the method's ability to isolate non-Gaussian properties in the absence of nonlinearity. Nonlinear Gaussian (Bottom-Left): Only the linear test is significant, successfully detecting nonlinear dynamics driven by Gaussian innovations. Nonlinear Non-Gaussian (Bottom-Right): Both tests are significant, correctly identifying the joint presence of nonlinearity and non-Gaussianity. Overall, this figure demonstrates how the combined use of maximum and median bicoherence statistics provides a robust framework for disentangling the distinct contributions of nonlinearity and non-Gaussianity in complex time series. Results Interpretation:

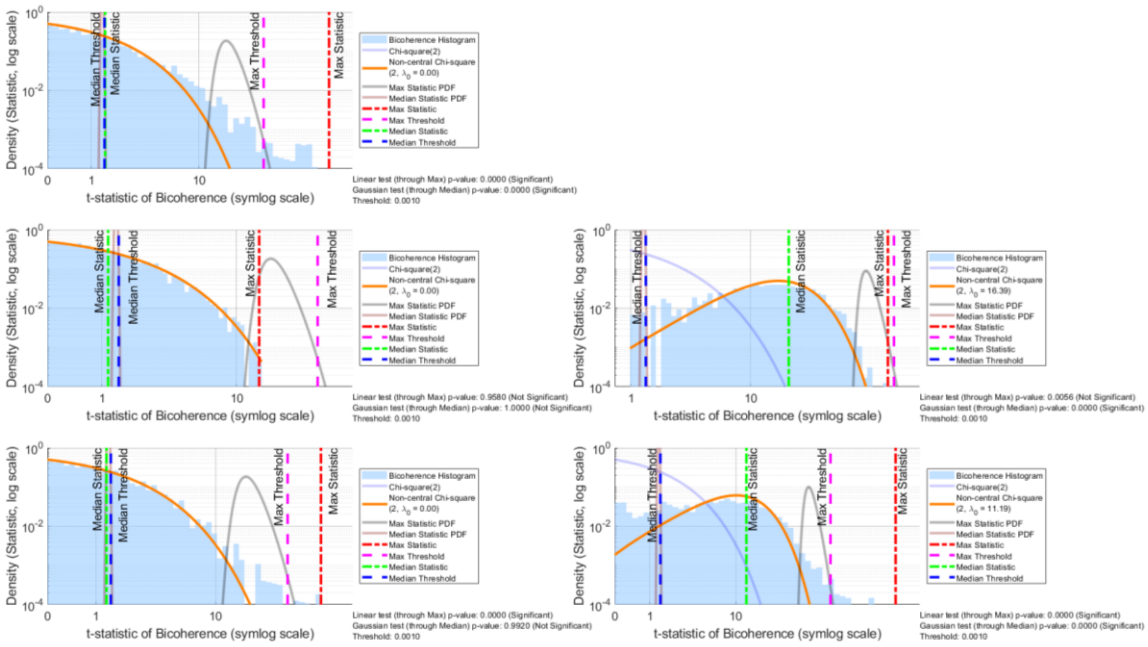

Figure A 3: Statistical analysis of bicoherence for real and simulated time series. *The figure displays the results of statistical tests applied to the bicoherence of five different time series signals to distinguish between nonlinearity and non-Gaussianity. The five cases are: (Top-left) Real intracranial EEG (iEEG) data; (Middle-left) A simulated linear Gaussian process; (Middle-right) A*

simulated linear non-Gaussian process; (Bottom-left) A simulated nonlinear Gaussian process; and (Bottom-right) A simulated nonlinear non-Gaussian process. Each subplot shows: Bicoherence Histogram (Light Blue): The distribution of the t-statistic calculated from the empirical bicoherence values of the signal. Chi-square Distributions: The theoretical central chi-square distribution with 2 degrees of freedom (blue line, $\chi^2(2)$), which is expected for a linear Gaussian process. A non-central chi-square distribution (orange line) is fitted to the data, where the non-centrality parameter (λ_0) captures deviations from the null hypothesis, related to non-Gaussianity. Statistic PDFs (Gray and Dark Red): The probability density functions for the 'Max' and 'Median' statistics, representing the expected distribution under the null hypothesis. Vertical Lines: The observed values for the 'Max Statistic' (red) and 'Median Statistic' (green) are compared against their respective significance thresholds, 'Max Threshold' (magenta) and 'Median Threshold' (blue). The text at the bottom of each plot summarizes two hypothesis tests: 1. Linear test (through Max): Uses the maximum bicoherence value to test for significant quadratic phase coupling, which indicates nonlinearity. A significant result occurs if the 'Max Statistic' exceeds the 'Max Threshold'. 2. Gaussian test (through median): Uses the median bicoherence value to test for a constant offset in bicoherence, which is characteristic of linear non-Gaussian processes. A significant result occurs if the 'Median Statistic' exceeds the 'Median Threshold'.

The result shows that the bicoherence can be different even if the second-order spectrum is similar. In the linear non-Gaussian scenario Figure A 2 ii, the data deviate from Gaussianity but do not exhibit intrinsic nonlinear dependencies. According to **Error! Reference source not found.**, this linear yet non-Gaussian structure typically manifests as a uniform or "constant" offset in the bicoherence. In other words, rather than showing localized peaks at specific bifrequencies, the bicoherence tends to exhibit a more diffuse elevation across the entire frequency domain. Conversely, the bicoherence in the nonlinear Gaussian scenario is limited to well-defined regions (i.e., specific bifrequencies where nonlinearity introduces phase coupling), with otherwise negligible values. This difference underscores that nonlinearity and non-Gaussianity can contribute distinctly to the observed cross-frequency coupling patterns, helping to explain why the bicoherence in the linear non-Gaussian simulation diverges markedly from that of real iEEG data.

We further fitted each case with our BiSCA model, which accurately reproduced both the power spectral density and bicoherence for each scenario (rows of *d* and *e* in Figure A 2). Notably, the model faithfully recapitulated the real iEEG features, mirroring the 1/f-like spectral decay and the subtle, significant cross-frequency interactions. These results highlight the model's capacity to disentangle and reconstruct complex neural signals, shedding light on the interplay of Gaussianity and nonlinearity that shapes iEEG dynamics.

A.3.2 Simulation for the Geometric view of bicoherence

The simulation of Figure 2 shown the geometric point of view of the bicoherence. The simulation employed a NNAR method to analyze nonlinear dynamics in intracranial iEEG data containing Wicket . The pipeline began with preprocessing a 2-second iEEG segment (sampled at 200 Hz) from a subject with normal variant activity. After reconstructing the phase space using a 23rd-order embedding, the NNAR

model was trained to capture the system's dynamics. A pruning step removed non-equilibrium states, retaining only key dynamics with weighted contributions exceeding 1e-2.

$$\mathcal{S} = \left\{ \boldsymbol{x}_k \mid \sum_{q=1}^{n_{eq}} w_k^{(q)} > \tau \right\}, \quad w_k^{(q)} = K_{h_k}(\| \boldsymbol{x}_k - \boldsymbol{x}_q^{eq} \|)$$

Deterministic and stochastic forecasts were generated using the pruned model. The deterministic (noise free) simulation to show the 3D phase portrait skeleton visualization, spectrum and bicoherence of this limit cycle. The stochastic forecasts with innovations modeled as Gaussian noise scaled by residual covariance to obtain potential landscape of 2D state space. The system's geometry was projected into 2D/3D state spaces via PCA of the high dimensional states set $\mathcal{S}$, and potential landscapes were estimated using kernel density methods on 100×100 grids, this is a nonparametric version of the landscape estimation R. Zhou et al., (2024). Spectrum and bicoherence, was implemented also with multitaper estimators ($NW = 2.5$) across 300-sample windows with 75% overlap.

To contrast with the asymmetric dynamics, we simulated symmetric nonlinear oscillations by enforcing the nonparametric state evolution function to satisfy $F(-\boldsymbol{x}) = -F(\boldsymbol{x})$,making the system dynamics invariant under state inversion $(\mathbf{X} \to -\mathbf{X})$. The modified state evolution becomes:

$$\tilde{\boldsymbol{x}}_{t+1} = \frac{F(\tilde{\boldsymbol{x}}_t) - F(-\tilde{\boldsymbol{x}}_t)}{2} + \tilde{\boldsymbol{u}}_t,$$

where the averaging ensures cancellation of even-order nonlinearities.

The reconstructed phase portrait revealed a stable limit cycle (Figure 2c), confirming the system's oscillatory nature. The potential landscape exhibited asymmetric minima (Figure 2d), explaining the spikes' directional morphology. Spectral analysis showed harmonically related peaks at 8.7Hz and 17.4Hz (Figure 2e), with total harmonic distortion (THD) -4.08dB. Bicoherence analysis demonstrated significant phase coupling between fundamental and harmonic components (Figure 2f), quantifying the nonlinear interactions. The symmetric version of the system, depicted in subplot (g) to (k), provides a contrasting perspective to the asymmetric case. Besides the symmetricity of the time domain analysis (g) to (i), the spectrum shows it only has the odd order harmonics, therefore, the bicoherence shows zero everywhere.

The asymmetric bicoherence profile (Figure 2f) reflects directionally biased nonlinear interactions, characteristic of depolarization-hyperpolarization asymmetry in the neuronal networks. The reconstructed limit cycle (Figure 2c) suggests possible self-sustaining oscillations stabilized by voltage-gated ion channel dynamics during the sample time interval. The potential landscape's asymmetry (Figure 2) aligns with the greater energy required for spike initiation versus termination, consistent with sodium channel inactivation kinetics. The 9 Hz spectral peak corresponds to thalamocortical resonance frequencies implicated in spike-wave generation. While the model successfully captured short-term dynamics ($\tau < 100$ ms), longer simulations showed phase drift, this could be introduced by the step of pruning removed the activities shifted by the slow variables, the underlying attractor may not perfect limit cycle but quasiperiodic or chaotic, suggesting the need for additional slow variables in future extensions (Stiefel & Ermentrout, 2016; Breakspear, 2017). These analysis bridges the spectral domain nonlinear analysis with the time domain evolution, providing a framework for quantifying stability landscapes in the nonlinear oscillations

The geometric interpretation of bicoherence provides critical insights into system dynamics. For an asymmetric system (Figure 2a-f), significant bicoherence between the fundamental frequency (8.7 Hz) and its second harmonic (17.4 Hz) signifies quadratic phase coupling. This interlocking of phases constrains the system's trajectory in phase space to a specific manifold, manifesting as an asymmetric "wicket" waveform and a distorted limit cycle in the phase portrait. Conversely, for a symmetric system (Figure 2g-k), the bicoherence is zero, reflecting the absence of phase coupling. The system's trajectory is unconstrained, resulting in a uniform limit cycle and a time-domain waveform with only odd-order harmonics. This contrast highlights how bicoherence geometrically quantifies the degree of asymmetry in the system's underlying potential landscape. Furthermore, bicoherence helps distinguish system-based nonlinearity from non-Gaussian noise. In a nonlinear system, the energy landscape imposes state-dependent constraints, suppressing noise-induced perturbations more effectively in regions with strong recovery forces (e.g., steep potential wells). This state-specific "filtering" of non-Gaussian inputs reduces the measured bicoherence compared to a linear system, where such perturbations propagate homogeneously (Figure A.2). This distinction underscores the importance of modeling both system nonlinearity and noise non-Gaussianity when interpreting higher-order spectral features.

The geometric interpretation of bicoherence reveals critical insights into the nonlinear dynamics of the system, particularly in how phase coupling shapes its oscillatory behavior. In the asymmetric system, the bicoherence plot (Figure 2f) shows significant phase coupling between the fundamental frequency at 8.7

Hz and its second harmonic at 17.4 Hz, indicating quadratic nonlinear interactions that constrain the system's trajectory in phase space to a manifold reflecting these phase-locked oscillations. This interlocking of phases manifests as the asymmetric morphology in the time-domain waveform of the Wicket (Figure 2a), with the directional bias corresponding to imbalanced phase relationships. The reconstructed phase portrait (Figure 2c) supports this, as these nonlinear constraints shape the stable limit cycle's trajectory. Conversely, in the symmetric system, the bicoherence is zero everywhere (Figure 2k), aligning with the regular, balanced oscillations in the time domain (Figure 2g) and the presence of only odd-order harmonics (Figure 2j). Here, the absence of phase coupling results in an unconstrained trajectory in phase space, producing a more uniform limit cycle (Figure 2h). This contrast highlights how bicoherence geometrically quantifies the degree of nonlinearity and asymmetry in the system's dynamics, linking spectral domain insights to the time-domain evolution and the underlying potential landscape (Figure 2d and 4i). These findings underscore the utility of bicoherence in analyzing stability and morphology in nonlinear oscillatory systems, offering a framework to explore the interplay between structure and dynamics.

A.4 Goodness of fit

To demonstrate how much variance can be explained by the model, here we put the cumulative density function of the R^2. In the formula defined in (13) and (15), the parameter $\{\mu_{\rho,k}\}$ has two options: 1) Harmonic fixed with the harmonic relationship of the "fundamental oscillation", 2) Free: initialize with spectrum and optimize the joint fit. We put the R^2 of both cases here.

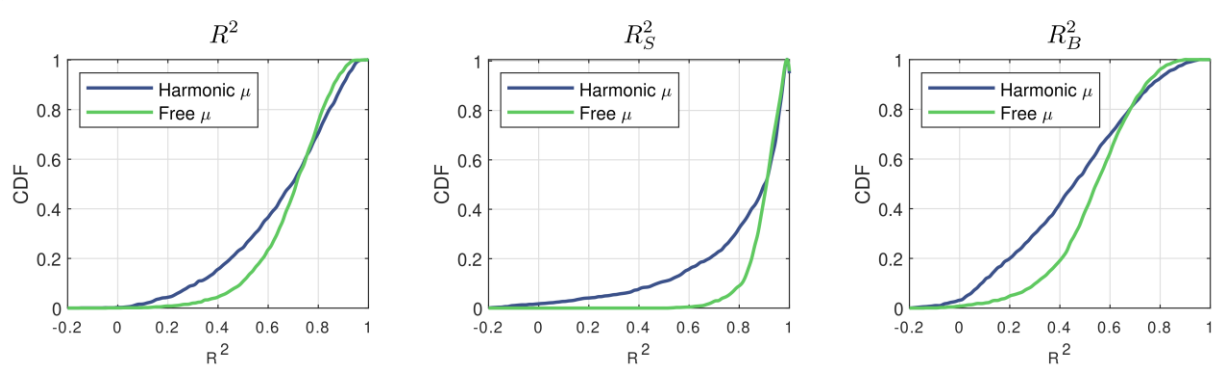

Figure A 4 Distributions of the coefficient of determination R^2 in three different conditions. *a) is the R^2 of the full model; b) is the R^2 for the spectrum; c) is the R^2 for the bispectrum*

The R^2 distribution is calculated for the fit of each channel shown in the Figure A 4. The goodness of fit suggests that the model's goodness of fit varies considerably across the entire dataset. The "free" option of the peak center fits with a greater degree of freedom. Therefore, its R^2 is concentrated on the right side, compared to the "harmonic" organized center peak option. Some phenomena, such as split Alpha, may not be described by the "harmonic" organized model.

Figure A 4 (a) shows a broad distribution of overall R^2 values, suggesting that the model's goodness of fit varies considerably across the entire dataset. A noticeable upward trend toward higher R^2 (up to ≈ 1) indicates that many data segments exhibit strong fits, although a small portion remains at the lower end of the scale. Since the variance of the spectrum and the variance of the bispectrum is quite different, which also vary with subject the R_S^2 and R_B^2 are more intuitive. Figure A 4 (b) R_S^2 are comparatively narrower near the high value but rise sharply toward $R_S^2 \approx 1$. This pattern implies that many single-subject spectral fits are quite robust, with fewer cases in the middle range of goodness of fit. Figure A 4 (c) presents a more bell-shaped distribution of baseline R_B^2 values. Most of these are clustered around moderate goodness-of-fit levels $R_B^2 \approx 0.4 - 0.6$, with fewer instances at the extremes (near 0 or near 1). Overall, bispectrum fits appear to be consistent but rarely reach near-perfect levels.

A.5 Peak relation from the spectrum

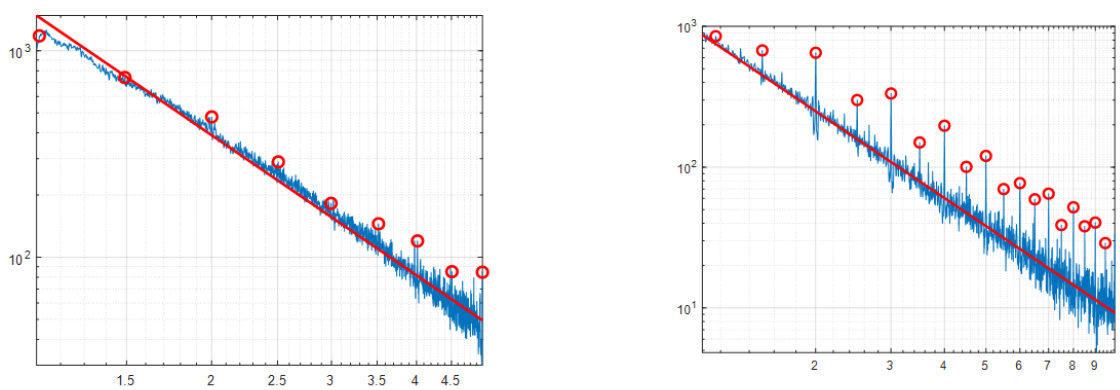

Figure A 5 the ratio of the peaks identified in the spectrum. *The left is from harmonized 1563 × 18 channels scalp EEG data. The right is from 1771 channels of iEEG data.*

Besides integer harmonic peaks of periodic oscillations, other proportions between peak frequency reveal possible quasi-periodic motion and chaotic; the distribution of the proportions showed possible scale free of the organization of peaks. On the Exponent Scale, the slope is 2.2531 for EEG and 2.0493 for iEEG. However, metaphysical models attempt to impose intriguing physical interpretations on empirical data without necessarily ensuring that these interpretations adhere to rigorous statistical or biophysical validity. Evertz et al. (2022) point out correctly that there is doubt that the aperiodic component is either "scale-free" or a reflection of criticality. An alternative is to look at biophysical models with effects of the extracellular space (Lindén et al., 2010) as mentioned by Evertz et al. (2022). In addition to interest and questions about the scale-free nature of ξ process (Bédard et al., 2006). This question was discussed in Valdés-Sosa et al. (1999) and Valdes-Sosa et al. (1999), when people argue that the EEG is chaos, the neural activity is a nonlinear stochastic system driven by the noise. We reserve these possibilities, and these conclusions still need to be verified by rigorous statistical methods. One possibility is that using the bicoherence in this paper to study the relationship between the components is possible when all the ratios here are the intermodulation combination of the integer peaks.